TRMM Precipitation Radar Reflectivity Profiles Compared to High-Resolution Airborne and Ground-Based Radar Measurements

G. M. Heymsfield

NASA Goddard Space Flight Center

Greenbelt, Maryland

B. Geerts

Science Systems and Applications, Inc.

Lanham, Maryland

L. Tian

Universities Space Research Associates

Seabrook, Maryland

For submission to Journal of Applied Meteorology

Corresponding author address:

Gerald M. Heymsfield, NASA GSFC, Code 912, Greenbelt, MD 20771.

ABSTRACT

In this paper, TRMM Precipitation Radar (PR) products are evaluated by means of simultaneous comparisons with data from the high-altitude ER-2 Doppler Radar (EDOP), as well as ground-based radars. The comparison is aimed primarily at the vertical reflectivity structure, which is of key importance in TRMM rain type classification and latent heating estimation. The radars used in this study have considerably different viewing geometries and resolutions, demanding non-trivial mapping procedures in common earth-relative coordinates. Mapped vertical cross sections and mean profiles of reflectivity from the PR, EDOP, and ground-based radars are compared for six cases. These cases cover a stratiform frontal rainband, convective cells of various sizes and stages, and a hurricane.

For precipitating systems that are large relative to the PR footprint size, PR reflectivity profiles compare very well to high-resolution measurements thresholded to the PR minimum reflectivity, and derived variables such as bright band height and rain types are accurate, even at high PR incidence angles. It was found that for, the PR reflectivity of convective cells small relative to the PR footprint is weaker than in reality. Some of these differences can be explained by non-uniform beam filling. For other cases where strong reflectivity gradients occur within a PR footprint, the reflectivity distribution is spread out due to filtering by the PR antenna illumination pattern. In these cases, rain type classification may err and be biased towards the stratiform type, and the average reflectivity tends to be underestimated. The limited sensitivity of the PR implies that the upper regions of precipitation systems remain undetected and that the PR storm

top height estimate is unreliable, usually underestimating the actual storm top height. This applies to all cases but the discrepancy is larger for smaller cells where limited sensitivity is compounded by incomplete beam filling. Users of level three TRMM PR products should be aware of this scale dependency.

1. Introduction

The Tropical Rainfall Measuring Mission (TRMM) satellite carries a spaceborne radar, providing real-time and climatological rainfall estimation (Kummerow et al 1998). In 1998-99 several TRMM field campaigns[1] were held to validate TRMM radar reflectivity and passive microwave data over tropical precipitation systems . The TEFLUN-A (TExas-FLorida UNderflight) campaign focused on springtime mesoscale convective systems (MCSs) mainly in southeastern Texas. TEFLUN-B was conducted in August-September 1998 in central Florida, in coordination with CAMEX-3 (Third Convection and Moisture Experiment). The latter focused on hurricanes, especially during their landfall, whereas TEFLUN-B concentrated on central Florida convection, which is largely organized by sea breeze circulations. Finally, TRMM-LBA (Land-Biosphere-Atmosphere interaction in the Amazon) took place during the first two months of 1999 in the southwestern quadrant of the Amazon Basin [2]. All experiments were amply supported by surface data, in particular a network of raingauges and radiosondes, a ground-based polarization radar, wind profilers, a cloud physics aircraft penetrating the storms, and a high-altitude aircraft (NASA ER-2 and DC-8 [TEFLUN-B only]), flying over the same storms. One of these aircraft, the ER-2, was equipped with visible, infrared and microwave imagers, electric field detectors, an interferometer, and the dual-antenna X-band ER-2 Doppler Radar (EDOP).

This study aims to assess how well the TRMM Precipitation Radar (PR) measures the vertical structure of a variety of precipitating systems. Of key importance to PR

[1] See http://trmm.gsfc.nasa.gov/trmm_office/
[2] See experiment plan at http://olympic.atmos.colostate.edu/lba_trmm/.

validation are TRMM-coincident aircraft flights over and within precipitating clouds, especially if these clouds are located within the network of ground-based instruments. Coordinated airborne/surface radar measurements provide high spatial and temporal coverage of precipitation systems covered by a single TRMM pass, thereby improving our understanding of how well TRMM measures rainfall from storms of various sizes, intensities and evolutionary stages. In particular, the segregation between convective and stratiform precipitation by means of TRMM-based criteria can be evaluated with high-resolution data.

TRMM PR data are calibrated and geolocated, and reflectivities are corrected for attenuation and partial beam filling. Furthermore, a range of qualitative and quantitative attributes is derived from the PR reflectivity profiles. The relative reliability of these data corrections and derived products can only be assessed through detailed validation efforts. One validation approach is to statistically compare TRMM products to independent data sets, such as ground radar, rain gauge, satellite IR, or sounding data. The statistical approach (e.g. Datta et al 1999) is justified by the sparse sampling nature of the PR, both in space and in time, making simultaneous comparisons too rare. Studies of this kind are facilitated by the monthly-mean products (level 3) provided by the TRMM Science Data and Information System (TSDIS). For instance, 3A-25 data are gridded monthly-mean PR-based rainfall estimates for the global tropics. The two data sets in any statistical comparison comprise distinct precipitation systems, but these 'individual' differences become insignificant when sufficiently large samples are compared. The availability of a statistically large enough sample of PR data is questionable in some regions and for some periods. More importantly, the data sets used in statistical comparisons, in particular rain gauge data, are only indirect measures of the PR measurements, thereby incorporating many uncertainties which remain even when the averages match very well.

In this study we evaluate the TRMM PR products by means of simultaneous comparisons against high-resolution reflectivity data in a small sample of storms. Of particular importance are EDOP measurements. EDOP is a non-scanning instrument with two antennas, one pointing to the nadir, the other pointing 33.5° forward (Heymsfield et al. 1996a). EDOP is an excellent PR validation tool, because of its high vertical and horizontal resolution, and also because, unlike ground-based radars, its nadir antenna has essentially the same perspective as the PR (Figure 1). The purpose of this paper is not to assess the accuracy of the PR calibration. Calibration tests are routinely undertaken by the Japanese Space Agency (NASDA) to evaluate sensor consistency and drift. Recent tests concluded that the PR is consistent with a calibration accuracy within 1 dBZ. EDOP data themselves underwent rigorous calibration tests, before and after the field experiments, and the calibration accuracy is believed to be much better than 1-2 dBZ. But the calibration issue is not the topic of this paper. Rather, the PR's vantage point, wavelength and other radar characteristics are significantly different from those of EDOP (Table 1), and these differences lead to several important differences in radar observations.

(1) *Horizontal resolution*. EDOP's beamwidth is ~3.0°, which in the nadir translates to ~0.5 km at 10 km altitude and ~1.0 km at sea level, when the ER-2 flies at 20 km altitude. Such resolution is sufficient to see shear-induced slopes in hydrometeor fallstreaks , as well as mammata-like anvil protuberances. The PR footprint size is about 4.3 km throughout the troposphere, increasing to about 5.0 km at the maximum

incidence angle (17°). Convective precipitation often falls from cells smaller than 4.3 km, in fact various studies suggest that less than a quarter of the rain cells have diameters larger than 4.3 km.. Sauvageot et al. (1999) found that radar-derived rain cell size distributions from various regions are exponential , with a slope of 0.3 to 0.8 km^{-1}depending on the rainrate threshold defining cells, range of cell sizes sampled, and meteorological factors. Cumulus cloud size spectrasuggest that this exponential relation is valid down to very small sizes (Wielicki and Welch 1986), smaller than can be observed in most radar studies. Goldhirsh and Musiani (1986) found that the median convective cell size near the mid-Atlantic coast of the United States is only 1.9 km. A minor related difference is that the EDOP sampling rate is 0.5 sec, resulting in an along-track sampling of about 100 m and an 80-90% overlap from one beam to the next. This yields higher beam-to-beam continuity and better resolution, since the pulse-volume averaged radar reflectivity represents a mean value at the center of the radar beam. No such oversampling occurs for the PR.

(2) *Sensitivity.* The TRMM PR's noise level (floor) is at --111 dBm (Bolen and Chandrasekar 1999); therefore the minimum detectable signal is approximately 18 dBZ. While this covers all rain rates down to about 0.4 mm hr^{-1} (assuming uniform beam filling), EDOP has a much higher sensitivity, allowing it to see the lightest rain, and most of the ice region of precipitating clouds. For instance, the spatial variation of stratiform precipitation sometimes is related to the location of generating cells or waves near the cloud top. The effects of limited horizontal resolution and low sensitivity combine to exclude isolated, small storm cells from the PR's view. To be seen by the PR, a cell with a diameter of 1 km needs to have an average reflectivity of

at least 33 dBZ (Figure 4 in Bolen and Chandrasekar 1999). If the cell is located off-center in the PR footprint, the required reflectivity would be even higher, as will be discussed in Section 2b.

(3) *Vertical resolution.* The EDOP range resolution is 37.5 m, compared to 250 m for the PR. This implies that the PR vertical resolution is equally-distributed over 250 m at nadir, decreasing to a 1,580 m deep layer at the outer incidence angle (17°) where the radar pulse-volume (a slice of 4.3 km x 250 m) is slanted at 17° from a level plane. As a consequence, detailed EDOP-derived bright band (denoted BB) profiles can be used to examine the ability of the PR to detect and characterize BBs at varying incidence angles.

(4) *Attenuation.* At 13.8 GHz the PR reflectivity profile suffers from significant attenuation in the lowest beam, both in convective and stratiform precipitation with peak reflectivities greater than about 35 dBZ. This threshold decreases slightly with increasing depth of the high-reflectivity layer, e.g. the path-integrated attenuation (PIA) is 5 dB for a 5 km deep layer. Attenuation rate (dB per kilometer) at the EDOP frequency (9.6 GHz) is about a factor of two less than at the TRMM frequency; for many situations, EDOP has minimal attenuation for reflectivities below about 45 dBZ (Caylor et al. 1995), or about 40 dBZ if these values are sustained through a deep layer, as commonly occurs in tropical deep convection. In this study we use attenuation-corrected PR reflectivity data (2A25), because the maximum layer-mean reflectivities exceed 35 dBZ in all but one of the cases examined here. EDOP data are not corrected for attenuation in this study because the maximum layer-mean reflectivities are below 45 dBZ in all cases.

Given these differences, one can treat EDOP cross-sections as high-resolution 'truth' for the TRMM PR. This implies that EDOP data can be 'degraded' to a PR perspective, and that degraded EDOP data from the various TRMM field campaigns can be used as a surrogate for the PR. This argument was a key motivation for the high-altitude remote sensing aircraft participation in the TRMM field campaigns (Zipser et al. 1999). TRMM overpasses are relatively rare and do not document the lifecycle of storms, therefore cloud microphysical modeling efforts aimed at improving TRMM precipitation algorithms and derived latent heating profiles will benefit from EDOP data as a complement to TRMM PR data. Furthermore, PR-observed features can be extrapolated to finer scales and to higher hydrometeor sensitivity by means of an inverted degrading process, however such process is not unambiguous. One such extrapolation is the estimation of the storm top height from PR data.

Of the four differences listed above, the first two are the most important. There is some concern that non-uniform beam filling (NUBF) has a systematic effect on PR reflectivity and hence rainfall and latent heating estimates. This concern has been addressed both with theoretical and observed echo patterns (e.g. Nakamura 1991, Amayenc et al. 1996, Testud et al. 1996, Durden et al. 1998), however real TRMM data have not been used until now. Durden et al (1998) used a scanning 13.8 GHz radar (the Airborne Rain Mapping radar or ARMAR) aboard the NASA DC-8 to simulate PR reflectivities in three dimensions. They found that degraded ARMAR data of tropical oceanic convection tend to overestimate the reflectivity near the cloud tops and underestimate the path-integrated attenuation. Amayenc et al (1996) also found some biases due to NUBF using nadir-looking airborne radar data of a rainstorm off the East Coast of the USA. Kozu and Iguchi (1999) proposed a correction to PR rainrate data due to NUBF, based on the local fine-scale rainfall variability as observed using ship-based radar data in the western equatorial Pacific. This variability can be correlated with a PR-measurable quantity such as PIA, however this correlation is probably not universally valid. In short, the de facto impact of sub-beam-scale convection and sharp reflectivity gradients on PR rain estimation and classification is not well understood and has not been analyzed by comparing PR data to high-resolution data.

In this paper, comparisons are made between the PR, EDOP, and ground-based radars for six TRMM overpasses during TEFLUN and TRMM-LBA. The emphasis of this study is on the comparison of the vertical patterns and profiles of EDOP and PR reflectivities, whereas the ground radars provide an independent check on the PR measurements. Other data, such as passive microwave measurements from the TRMM Microwave Imager (TMI) and the ER-2 mounted Advanced Microwave Precipitation Radiometer (AMPR) (Spencer et al., 1984), are only used in the interpretation of the PR-EDOP comparison. The physical relation between EDOP reflectivity cross sections and upwelling microwave radiances is explained in the case of a Florida thunderstorm by Heymsfield et al. (1996b). PR-derived products, such as BB characteristics and precipitation classification, are assessed as well, but the key PR variable in most other studies, i.e. surface rainrate, is not addressed here. Because of the small size of some of the selected storms, and the different viewing geometries and resolutions of the various radars, accurate mapping of these data to a common coordinate system is required. Section 2 describes the details of this mapping methodology. In Section 3, six examples are presented, covering a mainly stratiform frontal rainband), a convective cell in its decaying stage, a small, growing convective cell, a small mesoscale convective system (MCS), and a hurricane. Composite reflectivity profiles are compared in Section 4.

2. Methodology

2a. Viewing geometry, resolution, and beamfilling effects

Comparison of the PR with EDOP and ground-based radars involves data from drastically different viewing geometries (Figure 1). Both the PR and EDOP have high vertical resolution but blur the horizontal structure, while ground-based radars have excellent slant-range resolution but blur the vertical structure at increasing range. The ground radars themselves, i.e. S-POL, TOGA, and WSR-88D, have somewhat different range resolutions and beamwidths. Furthermore, the range gate values of reflectivity from the different radars are located at different locations in space and time. Comparison of data from these radars requires interpolation to a common reference frame with high accuracy geo-location. Two approaches are possible, each of which has merits. The first approach is to degrade all the data sets to the lowest common resolution volume. This volume has the horizontal dimensions of the PR footprint and the range-dependent vertical depth of the beam of the nearest ground radar. This allows for examination of differences between data sets all on the same, lowest resolution scale. This approach is ideally suited for calibration comparisons but it does not deal with the NUBF problem. The second approach is to interpolate all the observations to the coordinates of the highest resolution data (i.e., EDOP), in order to examine what reflectivity structures are present in each data set relative to the high-resolution 'truth'. The second approach is used in this paper, i.e. PR and ground-based radar reflectivities are resampled to a dense grid representing the beam and gate spacings of nadir EDOP data. One exception is the PR's vertical resolution, which is maintained at its nadir value (250 m). This approach is generally analogous to routine meteorological interpolation of upper air and surface observations to a grid for NWP model initialization. These data usually are widely-spaced relative to grid intervals and thus the interpolation method can be important in filtering and in reducing data aliasing (e.g., Trapp and Doswell 1999). The technique to interpolate the PR and ground-based radars to an EDOP section is described in Appendix A.

The largest cause of residual difference (i.e., not related to radar characteristics) between correctly geo-interpolated radar data is the non-simultaneity of the radar measurements. This difference needs to be minimized to address the effect of NUBF and other factors that distinguish PR data from EDOP data. TRMM measurements of a storm are essentially instantaneous, while ground-based radar volumes are collected in 3-5 minutes and EDOP data collected in ~8 min/100 km (Appendix B). During a time lag of a few minutes echo patterns can be displaced significantly, such as in hurricane conditions, and/or they can evolve, which is especially likely in small, short-lived convective cells. A better match than the ones presented in this paper could be obtained by correcting the data to a common time, i.e. the EDOP observation time. Temporal correction for advection is possible because of the 3-D nature of the PR and ground radar data, however advection vectors can not be readily estimated, and evolution is the more common culprit of differences in all cases presented here, except the hurricane. Such 'meteorological' (non-radar) differences emphasize the importance of simulating PR data by means of EDOP data, as discussed above. The details of the degrading process are described in Appendix B.1. In essence EDOP data are gridded to a vertical section and then degraded to the TRMM resolution by sampling it with a one-dimensional (along-track) representation of the PR antenna illumination function. This process accentuates differences in horizontal resolution between the PR and EDOP.

2b. Radar beam filtering.

It is well known that the radar antenna main and side-lobes cause distortion of a meteorological target (Donaldson 1964, Zawadski 1999). This is particularly true in sharp hydrometeor gradient regions viewed by ground-based radars, or vertical edges of storms viewed by the PR and EDOP. A more significant problem is the NUBF problems mentioned earlier. Both of these problems can cause a significant misrepresentation of the reflectivity. For simplicity, the filtering effects of a radar beam can be calculated in the following manner. Assume the true and measured reflectivity are defined by Z and Z_m, respectively, and the two-way antenna illumination function is represented by $I^2(\theta, \phi)$ where θ, ϕ are the two-dimensional angles off the antenna boresight. Additionally, the reflectivity variations along the slant range at range r are assumed constant, the circular radiation pattern (θ, ϕ) can be projected onto rectangular coordinates (x,y) in a beam-normal plane through the relations $x\text{-}X=r\theta$, and $y\text{-}Y=r\,\phi$. Here (X,Y) are the coordinates of the beam's center at range r, relative to the center of a storm cell (where x=y=0). We define $(\theta_o, \phi_o) = (2x_o\, , 2y_o)/r$ as the 3 dB (half-power) points of the radar antenna. Then the effects of beam filtering of the true radar reflectivity field may be given by:

$$Z_m(X,Y) = \int_{-\infty}^{\infty}\int_{-\infty}^{\infty} Z(x,y) I_*^2(x-X, y-Y)\,dx\,dy \tag{1}$$

$$I_*^2 = \frac{4\ln 4}{\pi x_o y_o} e^{-\left[\frac{(x-X)^2}{x_o^2/\ln 4} + \frac{(y-Y)^2}{y_o^2/\ln 4}\right]}$$

where I_*^2 is the normalized two-way antenna illumination function (e.g., Donaldson 1964). Clearly, this is a Gaussian distribution function, i.e. side lobe effects are ignored for this simplistic representation. The above relation is similar to Donaldson (1964) and others. Applying (1) to a nadir PR beam with $2x_o$=$2y_o$=4.3 km, we assume a true reflectivity field Z (i.e. a small storm cell) that is bell-shaped as well, with a maximum reflectivity of 50 dBZ:

$$Z(x,y) = Z_o e^{-\left[\frac{x^2}{r_c^2/\ln 2} + \frac{y^2}{r_c^2/\ln 2}\right]} \tag{2}$$

where r_c is the half-power radius of the true reflectivity pattern, and Z_o is the its peak value. Then Z_m can be derived as:

$$Z_m(X,Y) = A Z_o e^{-\left[\frac{X^2}{\frac{r_c^2}{\ln 2}\left(1+\frac{x_o^2}{2r_c^2}\right)} + \frac{Y^2}{\frac{r_c^2}{\ln 2}\left(1+\frac{y_o^2}{2r_c^2}\right)}\right]} \tag{3}$$

$$A = \left[\sqrt{1+\frac{x_o^2}{2r_c^2}}\sqrt{1+\frac{y_o^2}{2r_c^2}}\right]^{-1} \tag{4}$$

Here A provides information on the decrease of PR measured reflectivity with distance of the cell from the PR footprint's center, where this distance is expressed relative to the cell size, i.e. $(2x_o, 2y_o)/r_c$. For the case of a very narrow beam (i.e., $x_o, y_o << r_c$), then the measured reflectivity reproduces the true reflectivity. When the beam is broad relative to the size of the cell (i.e., $x_o, y_o >> r_c$), then $Z_m < Z_o$, and the true reflectivity distribution is broadened.

The variation of the PR measured reflectivity Z_m with cell size and location relative to the beam's center is shown in Figure 2a. Four cases range from when the cell is centered on the antenna illumination function (X=0), to when the cell is far off it (X= 3 km, which is just below the maximum distance between a cell and the nearest PR beam center). When the cell is larger than the PR footprint, the PR reflectivity approaches 50 dBZ. The PR reflectivity decreases faster-than-linearly with decreasing cell size, as well as with increasing distance between the cell and the PR beam center. For a large cell of 4.3 km diameter, the PR measured reflectivity ranges from about 49 dBZ for the cell centered on the illumination function (X=0) to 39 dBZ when it is far off center (X=3 km). For a medium-size (2 km diameter) cell, the reflectivities range from 47 dBZ (X=0 km) to 21 dBZ (X=3 km). The latter is very close to the PR noise floor. Of course if the cell is on the edge of one PR beam, the adjacent PR beam will measure a similar reflectivity from the same cell, i.e. the cell is broadened. The effect of this filtering on rainrates can be estimated by means of a Z-R relationship, e.g. $Z=260\ R^{1.38}$, for central Florida convection (Datta et al 1999). The maximum rainfall rate within the cell is 75 mm hr^{-1}. The PR rainrate from a 2 km cell is about 43 mm hr^{-1} when the cell is centered (X=0) and 1 mm hr^{-1} when the cell is far off-center (X=3 km) (Fig 2b). The average rainrate of the cell over the PR footprint area in this case is about 20 mm hr^{-1}, i.e. less than the PR estimate for a centered cell, but more than the PR estimate for a peripheral cell, even if this cell's rain is sampled by four adjacent PR beams. . If the median convective cell size is 1.9 km, as is the case for summer storms near the mid-Atlantic coast (Goldhirsh and

Musiani 1986), and if the distance between the centers of the cell and the beam is 1.5 km [i.e., the mean or most likely distance, $4.3/(2\sqrt{2})$], then the PR reflectivity is reduced about 11 dBZ from the peak cell reflectivity, and the PR rainrate would be about 20% of the peak rainrate in the cell.

In summary, storm cells and borders that are small relative to the PR footprint are broadened. The reflectivity deficit is larger for smaller cells and those off-center relative to the PR beam. The combination of filtering and limited sensitivity may cause weak cells, or the upper portion of stronger cells, to remain undetected by the PR. Storms larger than the PR footprint tend to be surrounded by an artificial weak-echo fringe. These effects have a direct impact on rainfall estimation. High rainrate events are undersampled and, because the illumination function and the Z-R relation are non-linear, the areal rainfall estimation may be systematically biased. Such bias can be expected when PR rainfall from the same algorithm is used in the comparison of a region with mainly small, scattered convection, such as central Florida, to a region with more organized precipitation systems, such as Texas.

2c. Rain type algorithms (convective, stratiform)

This paper utilizes the 2A25 reflectivity profile data, an 'operational' product, as well as 2A23 (PR-derived variables) and TMI data. All TRMM data are processed and archived at TSDIS. The TRMM PR product formats and algorithms are described in detail in NASDA (1999). 2A25 data are the result of several operations starting with the raw PR receiver data. These operations include quality control, clutter rejection near the surface, especially at high incidence angles and over mountainous terrain, referencing to an ellipsoidal representation of the Earth's surface, attenuation correction and NUBF correction. A hybrid between the Hitschfeld-Borden method and the surface reference technique is used (Iguchi and Meneghini 1994) to correct for attenuation. Relevant variables in the 2A23 data set include the presence and height of a BB, the rain type classification, and the storm top height.

Table 2 summarizes the classification scheme used in the 2A25 product. Rainfall is classified as stratiform if a BB exists ('V method') and/or the horizontal echo variation is small ('H method'). The 'H method' is an adaptation of the method by Steiner et al (1995) to the PR resolution: a beam is convective if its maximum reflectivity (Z_{max}) exceeds 40 dBZ or if Z_{max} stands out above the ambient echo. In the 'V method' rain is classified as convective if no BB exists and if Z_{max} >39 dBZ. Clearly the accuracy of the attenuation correction may significantly impact the rain classification. Both methods yield three outcomes (convective, stratiform, and inconclusive), and a combination of the H and V methods allows rainfall characterization in a probabilistic manner. For instance, if both H and V methods classify a pixel as stratiform, the 2A23 rain type is 'stratiform certain'. But if there is no BB yet the H method suggests stratiform rain, then the 2A23 rain type is 'probably stratiform' (Table 2). Sample tests indicate that the likelihood of correct BB detection is about 80% near nadir, decreasing to about 20% near the maximum scan angle of 17° (NASDA, 1999).

3.0 Comparison of TRMM with EDOP and ground radars

ER-2 flights coincided with TRMM overpasses over various types of precipitation systems. During TEFLUN A and B, CAMEX-3 and TRMM LBA, only nine

TRMM overpasses occurred while the ER-2 flew within the PR swath over precipitation, but only six of them were sufficiently data-rich and simultaneous for detailed comparisons. For each of the six cases, the ER-2 flight line near the time of the TRMM overpass was placed into the context of the horizontal radar echo pattern. The 2 km altitude image from the TRMM PR is shown together with a low level scan from the nearest ground radar in Figure 3 for all cases, covering a mainly stratiform frontal rainband (a, b), a convective cell in its decaying stage (c, d), a small, growing convective cell (e, f), a small mesoscale convective system (MCS) (g, h), and a hurricane (i-l). For this purpose, several ground-based radars were used that collected data during the TRMM overpasses. The S-band POLarization Radar (S-POL) radar from the National Center for Atmospheric Research (NCAR) participated in TEFLUN-B and TRMM-LBA. The TOGA radar supported by the Wallops Flight Facility participated in TRMM-LBA. Finally, the WSR-88D operational radars at Fort Worth, TX (KFWS), Melbourne, FL (KMLB), and Wilmington NC (KLTX), were used when possible to provide additional data for comparisons. All the ground-based radars were S-band (3 GHz) Doppler radars with 1° beamwidth antennas with the exception of the TOGA radar with a 1.6° beamwidth. The horizontal mapping procedures for ground radar and PR data are described in Appendix A.2 and A.3 respectively. The temporal coincidences of all relevant radars are listed in Table 3.

Comparison of vertical reflectivity cross-sections, which are the emphasis of this paper, are presented in Figs. 4-9. The EDOP panel (a) provides nadir reflectivity mapped onto a cartesian (x, z) grid above ground level (AGL). Each vertical column represents an EDOP beam at a particular surface latitude-longitude position. The vertical cross sections of ground-based radar (panel b)and PR (panel c) data were constructed using the mapping procedures described in Appendix A. Figures 4-9 also show profiles of various derived quantities for each case. These include: the brightness temperatures (10-85 GHz and 11 μm) from the TMI and VIRS (panel e), storm top height and BB height (2A23 product) (panel f), and PR incidence angle together with rain type (also 2A23) (panel g). These figures will be referred to in the subsequent discussion. The PR storm top height product (2A25) is the height of the first (highest) echo above the PR noise level. This height will be compared to the EDOP-estimated storm top, practically defined as the 0 dBZ contour. EDOP's sensitivity generally wass well below 0 dBZ.

3a. Widespread stratiform rain(21 April 1998)

A broad rainband, associated with a well-defined cold front oriented WSW-ENE, slowly propagates southeastward through central Texas on 21 April 1998. This rainband is over 700 km long, aligned with the cold front, and largely stratiform. Its cloud tops and rain rates decrease towards the northeast. The ER-2 flies along this rainband which also coincides with the PR swath of the TRMM overpass at 0634 UTC. (All times hereafter are in UTC.) At this time there are three short convective lines to the south and west of the ER-2 leg, most obvious in Figure 3a . These lines are oriented normal to the broad rainband and move along it, advected by strong westerly wind at 500 mb. They appear more vigorous in the PR image than in the KFWS radar PPI. The convective lines are at least 150 km from this WSR-88D radar, therefore their echo strength is weakened by attenuation and partial beam filling.

The ER-2 was directed to start just to the east of the westernmost of these three lines at 0624, thereby missing the two other lines to the north. By the time of the TRMM overpass about 10 minutes later, the westernmost line has moved into the ER-2 section. The PR reflectivity pattern matches EDOP's very well east of this line, as PR-EDOP coincidence improves to the east (Fig 4a). Some details are missed by the PR such as the sloping fallstreaks evident in the EDOP section below the freezing level. The fallstreaks are the result of the presence of a 25 ms^{-1} westerly shear between 0-5 km evident in the 00 sounding 6 h earlier at Dallas Forth Worth. The storm top height in the PR section is generally less than 1 km below the EDOP storm top, however during TEFLUN A the cloud top is likely higher than indicated since a EDOP sensitivity was reduced due to a amplifier malfunction. The algorithm-derived heights of the storm top and the BB (as shown in Figure 4f) verify well, and the rain east of the convective line (at the left edge of the panels in Figure 4) is classified correctly in the stratiform group. Compared to tropical stratiform rainfall systems (e.g. in hurricanes, section 3e-f), this rainband contains a large amount of ice, as evidenced by the 85 GHz upwelling radiance. This is not because of high cloud tops (merely 8 km) but because the freezing level (~3 km altitude) is about 2 km lower than in the tropics. Over much of the rainband the 85 GHz brightness temperature, as measured by the TMI and AMPR, is below 220 K. McGaughey et al (1996) find that 220 K is the minimum 85 GHz brightness temperature associated with ice scattering in stratiform regions of tropical oceanic systems. Passive microwave temperatures from lower frequencies (especially 19 and 10 GHz) are only marginally depressed (Figure 4e).

<u>3b.</u> The trailing edge of a dissipating convective cell (13 August 1998)

This case illustrates a borderline feature for the PR, mainly in terms of sensitivity, and there is a significant reflectivity gradient across the EDOP section. The ambient wind is weak at all levels on 13 August, and it is mainly westerly (<8 m s^{-1}) below 10 km. Afternoon thunderstorms develop, mainly along outflow, sea breeze and river breeze boundaries. About 15 km inland from the Banana River, a sequence of short-lived thunderstorms builds discretely southward and dissipates from the north. The ER-2 flies from west to east across the northern edge of a storm cell (Figure 3c). The EDOP reflectivity is low at all levels (Figure 5a), and there is a suggestion of a weak BB. The PR, recording this storm 1 (right) to 4 (left) minutes later, can see the storm cell, even some of its decaying anvil (Figure 5c). The PR storm top, just below 10 km, is about 2 km below the actual storm top (Figure 5f). The PR can see the rain reaching the ground. This rain is classified correctly as 'probably stratiform', because of the H-method (the echo is too weak for it to 'stand out'), not because a BB is detected. The BB is not detected because it is quite weak and because the PR incidence angle is fairly large (8°).

The PR only marginally detects the smaller but more intense shallow cells to the west (x<10 in Figure 5), about 4 minutes after the ER-2 passage. The AMPR brightness temperatures at 10 and 19 GHz are lower than at 85 GHz for these cells, suggesting that they contain very little ice. This PR detection failure may be affected by NUBF, however the degraded EDOP image (Fig 5d) suggests that the PR should still capture a clear signal. The more likely cause is the rapid decay of these shallow, isolated cells. In the 2225 S-POL volume, shown in Figs 3d and 5b, these cells are much stronger than in the

2231 volume (not shown). Another factor may be the across-leg reflectivity gradient (i.e., normal to the cross-section) apparent in Fig 3c .

3c. Small convective cell (1 February 1999)

Many convective towers formed in the afternoon of 1 February 1999 over Rondonia, Brazil, but they were generally small and short-lived. EDOP recorded 12 cells with at least 40 dBZ at an altitude of 2 km during a 3 hour flight period (1730-2030). With the exception of a 30 km wide storm overflown twice, the average diameter of these cells was 5 km (measured between the 20 dB EDOP boundaries at 2 km), i.e. about the size of the PR footprint. The sample is somewhat biased because the ER-2 targeted the larger thunderstorms in the population. The tops of these storms were not very high, but variable (5-9 km), and no spreading anvils nor stratiform regions formed. The minimum 85 GHz brightness temperatures of the first five of these cells was only 240-260 K (AMPR failed at 1842). Organized deep convection did not develop on this day, probably because of a lack of wind shear. Between 0-5 km, the wind was weak (less than 10 m s^{-1}), mainly from the northeast. Easterly shear of about 25 m s^{-1} existed between 5-11 km, and this was evident in the shearing of the tops of some taller cells.

At the time of the TRMM overpass, the ER-2 flew near the western edge of a line of convective cells, about 40 km long and 5-10 km wide. This line is captured both by the S-POL PPI and the PR CAPPI in Figure 3e-f. The line is moving southward and growing in length, but the cell at 30 km in Fig 6a (visited twice by EDOP) is dissipating (Figure 6a) but still has a narrow intense core with very few hydrometeors above 5 km and no anvil. The S-POL section (Figure 6b) is almost identical to EDOP's, but with lower vertical resolution. The PR detects this cell, located close to the TRMM nadir, about 6.6

min later (Figure 6c), but the maximum reflectivity is about 30 dB (as opposed to 45 dB) and the storm top is near 5 km (as opposed to 12 km). The degraded EDOP (Figure 6d) shows a stronger and slightly deeper echo pattern than the PR. The difference may be partly explained by cell evolution. When the ER-2 returns along this section over this cell, about 6.8min after the TRMM passage (not shown), the maximum reflectivity is still about 38 dB and the echo top about 10 km. The minimum AMPR 85 GHz brightness temperature of this cell is about 240 K, but the TMI brightness temperature traces don't record any significant disturbance over the cell (Figure 6e). The VIRS does see the cell clearly, with a minimum IR temperature just below 225 K (i.e. a storm top just above 11.5 km),. The main cell is classified as 'other' and 'probably stratiform', not because of a BB, but because of low PR maximum reflectivity. The size and strength of this feature, as revealed in EDOP imagery, makes it clearly convective,.

The weak cell to the north of the main cell along this flight leg, near x=50 km in Fig 6a, offers a nice example of detection failure due to the PR's sensitivity threshold. The degraded EDOP image (Fig 6d) suggests that the PR should just detect it. The PR does not see it, probably because at the time of the TRMM overpass (5 min later), this feature has weakened further, as suggested by the ER-2 return flight along this leg and S-POL imagery. The only TRMM probe that records this weak feature is the VIRS (Fig 6e). From a rainfall perspective, this weak feature is insignificant, since most or all rain appears to evaporate before reaching the ground.

3d. Small MCS (23 February 1999)

A broken line of cells grew into a continuous line over 100 km long between 1900 and 2000 on 23 February. This line was oriented NNW-SSE and propagated southeastward at first but later stalled. Convection along this line was most vigorous between 2000 and 2030, then weakened and a trailing stratiform region formed to the northwest. By 2200 all convection had disappeared and a ~3,000 km^2 large area of stratiform rain remained. This area expanded and intensified somewhat during the next half-hour, and then dissipated during the next two hours. The ambient wind below 5 km altitude was mostly northwesterly at 7-15 ms^{-1}, an easterly jet was found at ~13 km. The easterly wind above 7 km probably supported the formation of the westward-trailing stratiform region.

Figure 3g-h shows this line in a maturing stage. Convection is found mostly to the south along the leading (eastern) side of the line, while the northwestern portion develops into a stratiform region. The EDOP section essentially runs along the leading line of convection. No BB is present in this section (Fig. 7), except in the far south where some remnants of the shorter-lived southern portion of the line can be seen. The reflectivity generally drops off rapidly above the freezing level in this section, and convection is not very deep. The AMPR data indicate that much ice is transported to the west of the line (i.e. into the page of Fig. 7a). The minimum AMPR 85 GHz brightness temperature is about 160 K in this section, but 135 K over the stratiform region. Higher altitude CAPPIs from the PR (not shown) confirm that at 8 km the echoes are strongest to the west of the ER-2 track, while at 2 km they are strongest on the track or just to its east. This is consistent with the observed growth of the stratiform region. The deepest echo in the EDOP cross section (at x=40 in Fig. 7a) are actually in the lee of an active cell to the east of the line, so stratiform intensification processes (i.e. mesoscale updraft and ice growth above the freezing level, Houze 1993) may be active in this part of the cross section.

The ground-based radars (Figs. 7b,c), especially TOGA (which is closer), match the EDOP section well. The height, intensity, and structure of the PR echo also compares well to degraded EDOP echo pattern (not shown), because the EDOP-PR sampling time difference is small, less than 3 min throughout this section. The small discrepancies are mainly due to across-line gradients (i.e. the third dimension)..

PR rainfall is classified as 'certainly convective' to the south and 'probably stratiform' to the north (Fig. 7g). The classification as stratiform is not due to a BB (neither the PR nor EDOP detect a BB) but to weak reflectivities. This northern (right-hand) region appears convective from an EDOP perspective, because of high reflectivities and their gradients, and an absence of a BB. However this region is just to the east of a large area which clearly is stratiform. [I guess we are not verifying the TMI] The PR storm top height (Fig. 7f) is close to that of other radars, except to the south (x<15), where stratiform and dissipating clouds have higher tops (EDOP, TOGA, and S-POL in Figs. 7a-c) between 8-10 km. In fact even the PR (Fig 7d) has higher tops than the algorithm-derived storm top, which in this area (x<15) is below the freezing level.

3e. Hurricane Bonnie Pass 1 (26 August 1998)

EDOP data were collected during three TRMM passes over Hurricane Bonnie on 26 August 1998. At the time of the overpasses (1137-1451), Bonnie's central pressure was steady at ~ 965 mb, and its maximum sustained surface winds were about 50 ms^{-1}.

Bonnie made landfall near Wilmington NC around 0330 27 August. [3]At the time of the EDOP observations, Bonnie had one or more weak and ill-defined inner eyewalls and a stronger and more continuous outer eyewall with a diameter of ~170 km. Only the first and third TRMM passes are discussed here, because the PR swath of the second one missed Bonnie's eye and only a short section of high-incidence PR data coincided with the EDOP section. Note that the PR algorithms correctly detect and place the BB even at high incidence angles.

The first TRMM pass, at 1137, is almost exactly over Bonnie's eye (Fig. 3i-j). Several rain arcs can be seen in the region surrounded by the outer eyewall, and the PR captures all but the finest features present on the WSR-88D PPI, such as the shallow radial bands at the northwestern margin of the storm. The EDOP section lags the TRMM section by 13-35 minutes (Fig 8).. The difference between the PR section (Fig. 8c) and the corresponding degraded EDOP section (Fig. 8d) is largely due to this time lag, and is most obvious inside of the outer eyewall, where echoes are more transient. A much better fit could be obtained if advection of the hurricane is accounted for, but this correction is beyond the scope of this discussion.

The EDOP section (Fig. 8a) displays some fine scale features which are beyond the resolution or sensitivity of the PR. This includes: the spreading of the anvil outward from the outer eyewall, thin rain columns within the outer eyewall, and low-level radial confluence suggested by the inwardly curved fall streaks in the rain layer on both sides of the eye (which is near x=280 km). Otherwise the PR-EDOP comparison is excellent for the outer eyewall, including its BB and outward slant.

---

[3] See the Preliminary Report by NHC at http://www.nhc.noaa.gov/1998bonnie.html.

In this section most rain is correctly classified as 'certainly' or 'probably stratiform' (Fig. 8g). The PR storm tops of the deeper features are 2-4 km lower than EDOP heights. The lowest TMI 85 GHz brightness temperature associated with outer eyewall (near x=190 km) is only 240 K (compared to 220 K for AMPR), i.e. rather warm compared to continental convection, such as the small MCS discussed in Section 3d. The high 85 GHz temperatures and low reflectivities above the freezing level implies an absence of significant ice scattering. This is common for tropical oceanic MCSs (McGaughey et al 1996). The more shallow rain echoes within the inner eyewall remain undetected at 85 GHz, both in TMI and AMPR data. Other hurricanes with a double eyewall structure, such as Gilbert (1988), reach their greatest depth and intensity in the inner eyewall (Dodge et al 1999)..

3f. Hurricane Bonnie Pass 3 (26 August 1998)

At 1450 Bonnie's outer eyewall has contracted slightly, and the inner rain arcs have weakened a little (Fig. 3k-l). While most of the hurricane's rainfall field is northeast of the eye, the outer eyewall is most intense towards the southwest. The ER-2 flies from NE to SW across the eye, but the PR swath misses the northern part of the outer eyewall. The EDOP cross section (Fig. 9a) confirms the asymmetry, with a highly tilted yet weak northeast eyewall, a deeper southwest eyewall, with the eye centered near x=150 km. Many shallow but intense echoes can be seen within the outer eyewall in the EDOP pass. Ground radar and PR CAPPIs (Figs. 3k-l) also indicate that these cells have echo tops that are close to 6 km, however some cells inside the outer eyewall are much deeper.

The PR section detects a deep cell (x=170 km in Fig. 9c) and when the ER-2 flies overhead about 10 min later, this cell has largely been advected out of the cross section. Therefore the degraded EDOP echo is weaker than the PR echo; otherwise the PR-EDOP correspondence is quite good. The PR BB height is similarly to EDOPs except that it is slightly higher within the eye than in the eyewall (Fig. 9f). This elevated BB height is due to a higher 0°C isotherm within the eyewall. This feature can also be seen in pass 1 (Fig. 8f), but it is not as pronounced. The cloud height derived from the PR is generally below the EDOP and actual cloud height. This is apparent in the outer eyewall (x=170-200 km) where the PR storm height is 2-4 km too low. Some fallstreaks below 5 km altitude (120 km <x<150 km)) with a maximum reflectivity of ~25 dB are too thin and/or too weak to be seen, so no PR cloud height was assigned.

The rainfall classification scheme is excellent, even at high incidence angles. Overall, a BB is detected correctly by the PR algorithm. Areas classified 'certainly stratiform' (x=170-190 km) appear clearly as stratiform in EDOP imagery, and for the two areas classified as convective, EDOP does not reveal a BB. The 85 GHz brightness temperatures measured by the TMI are only barely depressed by the shallow cells inside of the outer eyewall, but they are as low as 205 K over the southwestern outer eyewall (Fig. 9e). These data correspond well to those of AMPR.

4.0 Comparison of the statistics of the profiles.

Mean height profiles of reflectivity were constructed (Fig. 10) for the cross-sections shown in Figures 4-9. These profiles were obtained by first converting reflectivities in "dBZ" to linear units before averaging across each height level (0.0375 m for EDOP and ground-based radars and 0.25 km intervals for the PR). To focus the comparison on the same precipitation structures, reflectivity profiles from radars other than the PR are thresholded to the PR's minimum detectable reflectivity of 17 dBZ. Mean profiles for ground-based radars had to be truncated near the ground because the upward slanting of the lowest beam away from the radar caused a bias in the averaging length at a particular level. Much information is lost in the reduction of a precipitating system to a mean profile, but the comparison of the first moment only from various radars is more feasible than that of CFADs (contoured frequency by altitude diagram, Yuter and Houze 1995) or other distribution functions. The comparison of mean profiles is useful for calibration purposes but the focus in this study is on the details of the profiles. For instance, how does the thickness and the strength of the BB in the PR compare to that of EDOP and that of ground radars? How does reflectivity change with height below the BB, and what cloud microphysical consequences can be drawn ? How do profiles compare in the case of NUBF ?

The vertical filtering due to the PR's gate spacing and off-nadir viewing results in a underestimation of the BB strength of 3-9 dBZ (Fig 10a and f). The PR BB height matches that of EDOP very well, but it should be cautioned that the bright band thickness in both the PR and EDOP is likely overestimated due to averaging over an extensive region. EDOP often observes bright band thicknesses much less than the 250 m pulse volume thickness. The effect of NUBF is illustrated well in the profiles of Fig 10d: the PR estimate is 4-10 dBZ below that of EDOP and S-POL, and the reflectivity-based cloud top is much lower. For small or rapidly evolving storms, a good temporal match is essential. Figure 10c shows the collapse of the trailing part of central Florida convection evidenced by the rapid 4-8 km altitude reflectivity decrease from 22:19 and 22:31 UTC. Part of the observed reflectivity differences in Fig. 10c are the result of the flight line crossing a strong gradient region of reflectivity. The TRMM footprint is relatively large and hence may sample this region differently than EDOP and S-POL. The discrepancies in the hurricane cases (Fig 10f) are also largely due to non-simultaneity; in this case advection mentioned earlier is likely the cause of some of the differences. For all the cases presented, the best time coincidence occurred for the small MCS on 23 February 1999 (Fig 10e). The reflectivity profile differences for this case are largely due to calibration differences and also PR attenuation correction and NUBF algorithms. Clearly the PR profile nicely matches the S-POL and EDOP traces.

5. Summary and Conclusions

In this paper we compare horizontal and mainly vertical reflectivity structures from the TRMM PR 2A25 product to data from higher-resolution, more sensitive radars, both airborne (i.e., EDOP) and ground-based. In the comparison, ground radar and PR data are interpolated to an earth-relative cartesian grid, as well as in the geo-located cross-sections covered by EDOP beams. This exercise is not trivial because of different beam geometries, resolutions, earth references, and the ER-2 aircraft motions, but it is essential for the validity of point-to-point comparisons. Both the PR and EDOP view precipitating systems from (near) zenith, yet there are several significant differences, the most important one being the horizontal resolution.

This study has intentionally not focused on calibration differences between radars since these differences will mainly shift profiles by a constant reflectivity over most of the reflectivity dynamic range. Instead, the emphasis is on the shape of the profiles, and its dependence on storm size and type.. The comparisons yield highly favorable agreement of the PR with EDOP and the ground radars for large precipitation regions. It is known that a significant portion of the rainfall results from convection that is small relative to the PR footprint, and that PR reflectivity profiles and rainrate estimates depend on storm size. In fact a correction for NUBF is applied operationally in obtaining the 2A25 product. Simple calculations show that the PR-measured reflectivity, and hence rainrate, becomes increasingly reduced, not only as the storm cell size decreases, but also as the cell is displaced further from the PR beam center. The effects of beam filtering and limited sensitivity compound to make small and/or weak cells entirely or partly undetectable by the PR, and the render PR statistics of derived variables such as storm type and rain type unreliable for small systems. A bias is possible also for larger (convective) systems, because of the typically high reflectivity gradients along storm edges. PR broadening of such gradients results in an artificial fringe around convective storms. In particular users of Level 3 (monthly-mean) TRMM PR products should be aware of the strong scale dependency of PR estimates. At Level 3, the scale dependency is impossible to assess because spatial information of individual storms is lost in the processing from instantaneous to mean rainrates.

It is a rare event when a TRMM overflight is within a few minutes of a straight-and-level ER-2 flight leg, a ground-based radar volume scan, and a precipitating system of interest. In fact the differences in presented reflectivity cross sections derived from the various radars are largely due to non-simultaneous sampling (allowing significant advection and evolution). Six cases from TEFLUN (A and B), CAMEX-3 and TRMM

LBA were judged to be sufficiently simultaneous and data-rich for a radar intercomparisons. These cases represent various meteorological situations: a broad, mostly stratiform rainband, a hurricane, a small MCS, a dissipating convective storm, and a small yet active convective cell. Some preliminary conclusions can be drawn from this small sample of EDOP-TRMM coincidences:

- High resolution EDOP reflectivity sections show that the TRMM PR, given its resolution and sensitivity threshold, captures most of the spectrum of sizes and intensities of precipitating systems very well, in terms of both 2A25 vertical reflectivity structure and deduced variables.
- The PR accurately detects bright bands, their depth and their height, in fact in this regard it outperforms WSR-88D radars at typical operating ranges. High-resolution vertical reflectivity profiles from EDOP suggest that the PR rainfall classification is realistic, even at high incidence angles.
- EDOP (as well as other airborne radars such as ARMAR) reflectivities can be degraded to provide a TRMM PR surrogate for simulation/retrieval studies. While the viewing geometries of the EDOP and AMPR are different than those for the PR and TMI on TRMM, the ER-2 can be focused on a specific storm of interest to provide insight on the performance of TRMM during this situation.
- The vertical structure, intensity and rainfall classification of convective cells smaller than the PR footprint may be erroneous. For sub-PR-footprint cells which can be common in the tropics, underestimation of reflectivity and storm top heights can result in mis-classification of convective precipitation as stratiform.

- The limited PR sensitivity results in the failure to detect weak precipitating systems and small convective cells; storm top heights are also underestimated, especially in tropical stratiform regions where reflectivity profiles fall off rapidly with height.

Further work is aimed at a more detailed comparison and evaluation of TRMM products, including attenuation and surface reference (σ^o), as well as microwave radiances.

Acknowledgements

This work was supported under NASA's TRMM program managed by Dr. Ramesh Kakar at NASA Headquarters. There are a number of key people in field campaign operations that deserve special credit. Dr. Ed Zipser and Ms. Robbie Hood worked jointly with the primary author in directing ER-2 flights during the TEFLUN-B and CAMEX-3 campaigns, Dr. Steve Rutledge, Dr. Ed Zipser and Walt Peterson directed TRMM-LBA ER-2 flights. Dr. Vivekanadan Dr. Ed Brandes, and others, were key in the S-POL radar science direction during ER-2 flights. Dr. Steve Bidwell and Mr. Ed Zenker are greatly appreciated for the superb engineering effort on the EDOP instrument. We are appreciative to Dr. Bob Meneghini for many excellent science discussions, to Mr. Carlos Morales and Dr. Liang for guidance on reading PR and other TRMM data sets. Radar data and assistance was provided by Mr. Dave Wolff (TOGA) and Mr. Bob Rilling at NCAR (S-POL). Many others answered the many small questions that arose due to the diverse nature of the data sets used in this paper.

Appendix A: Mapping algorithms.

An accurate interpolation of all the radar data sets into a common (earth-relative) coordinate system is essential before the various data sets can be compared. The coordinates of the EDOP flight line images are chosen as this common frame of reference, as described in section 2. The EDOP mapping is briefly described in Appendix A.1. Ground-based radar and TRMM PR data are three-dimensional, and their mapping onto a level, uniformly-gridded plane, as well as to the EDOP section, is described in Appendices A.2 and A.3 respectively. The redistribution of two-dimensional (horizontal) TRMM data is described in A.4.

A.1 EDOP Coordinates and mapping.

The ER-2 tracks presented in this paper are relatively linear although occasionally there are small aircraft heading adjustments (such as on pass 1 on 26 August 1998, Fig 3i) or other more minor deviations in heading due to cross wind variations at altitude Thus to retain accuracy in the mapping of other data sets, each beam of EDOP data is assumed to be normal to the earth's surface and each gate has an associated position (δ, α, z) where δ is latitude, α is longitude, and z is height above the earth's surface. This assumption is quite good since the ER-2 is relatively stable during flight with roll excursions of less than 0.25° (i.e ±175 m on the ground) and pitch excursions of less than 1°. The coordinates of gates in each beam at ~100 m intervals along the flight track are then gridded in (x, z) such that pixels in a single vertical column represent a single dwell of data, and the x axis represents dwells along the flight line. In all cases presented here the height of the earth surface is less than 200 m above mean sea level, so EDOP heights are not corrected to represent altitude above sea level.

A.2 Ground-based radar mapping.

Ground-based radar data are collected in spherical coordinates [(r, ϑ, ϕ) where r is range, ϑ is azimuth, and ϕ is elevation] and are mapped to EDOP vertical sections using the transformation equations developed in Heymsfield et al. (1983). These "small range" equations are applicable to distances less than about 200 km from the radar and can be summarized as follows:

$$s = \frac{r\cos\phi}{(1+(r/R')\sin\phi} \qquad \text{(A1)}$$

$$x = s\frac{R}{R'}\sin(\theta) \qquad \text{(A2)}$$

$$y = s\frac{R}{R'}\cos(\theta) \qquad \text{(A3)}$$

$$\alpha = \alpha_s + \frac{x}{R\cos\delta} \qquad \text{(A4)}$$

$$\delta = \delta_s + \frac{y}{R} - \frac{x^2}{2R^2}\tan\delta_s \qquad \text{(A5)}$$

where R is the local radius of the earth at the radar station, the effective earth radius $R'=4R/3$, (x,y) the radar-relative horizontal location, and the subscript s refers to the radar location. These approximations provide (δ, α, z) to within a few tenths of a km at 200 km from a radar. The topographic height of the radar above sea level is ignored.

Using the above equations, the (r, ϑ, ϕ) location from a given radar is calculated for each EDOP pixel. Then, for each pixel, a search is performed over the radar volume scan for the 8 surrounding gates (4 each from the elevation scans above and below ϕ). Interpolation is performed using trilinear interpolation, i.e., first the reflectivities are interpolated bilinearly to (r, ϑ) on each elevation scan, and then these values are linearly interpolated along ϕ. It should be noted that the reflectivites in "dBZ" are linearized before the interpolation and converted back to dBZ after the interpolation. While better interpolation schemes exist, the linear interpolation, also used in Heymsfield et al. (1983), is simple to implement and provides reasonable results. Trapp and Doswell (1999) address the ramifications of using bilinear versus Cressman and Barnes interpolation which have more easily understandable filtering responses.

The ground-based radar PPI scans shown in Figure 3 are constructed using an almost identical interpolation approach to the above and in Heymsfield et al. (1983). This approach uses equations A1-A5 and interpolation to a regular latitude-longitude grid with intervals of 0.01° in latitude and longitude.

A.3 TRMM PR mapping

The PR reflectivity data used in this study is based on the 2A25 product provided by TSDIS. This product includes attenuation-corrected reflectivity and rain rate profiles, and geolocation information. The reflectivity profiles have high range resolution (250 m) and coarser (~4.4 km) beam spacing. For simplicity, the PR profiles are assumed vertically oriented even though they can be tilted up to about 17° scan angle. This implies that an echo at the edge of the PR swath at 15 km altitude would be displaced about 4 km (i.e. one PR pixel spacing) horizontally from the surface position of the profile, towards the TRMM nadir position. In most cases, this is not a problem since the PR scan angles are usually much smaller and the echo heights are less than 10 km. Thus, each range gate has a (δ, α, z) location.

Interpolation is performed as follows. For each EDOP profile which has an associated (δ, α, z) coordinate, a search is performed on the TRMM data for the four profiles surrounding this (δ, α) location are identified. Then Cressman interpolation (Cressman, 1959) is applied to these profiles, level by level in the PR profile at 250 m intervals. The resulting interpolation function is given by:

$$Z_{edop} = \sum_{i=1}^{4} \frac{\kappa^2 - d^2}{\kappa^2 + d^2} Z_{PR} \tag{A6}$$

where κ=5.0 km is the influence radius, d, the distance from the EDOP pixel location, and Z_{edop} and Z_{PR} are the EDOP and PR reflectivities, respectively. This function is a relatively simple objective analysis function, yet it captures most of the PR features well in the interpolated vertical sections. This interpolation was compared with using the nearest point to the EDOP pixel and the interpolation approach was superior. The radius of influence was chosen as the minimum value for which $d<\kappa$ for at least 4 PR pixels anywhere. It is not much larger than the spacing between PR samples, so the Cressman interpolation applied here is applying minimal smoothing of the data. Discontinuities in the PR data displayed on the EDOP mesh arise from the jump from one PR beam to another. These discontinuities are much smaller than in the 'degraded' EDOP data because the latter represent the PR resolution (Appendix B) and are not distributed on the fine EDOP mesh.

The constant-altitude PR echo maps shown in Figure 3 are constructed using a standard Delaunay triangulation scheme to map irregular gridded points to a regular latitude-longitude grid with a grid mapping interval of 0.02° in latititude and longitude.

A.4 Mapping of two-dimensional TRMM parameters

Many of the TRMM parameters are located only by their latitude and longitude, not by their altitude, for instance the TRMM Microwave Imager (TMI) brightness temperatures (2B11), the Visible and Infrared Scanner (VIRS) infrared temperatures (1B01), the path integrated attenuation (2A21), rain type (2A23), normalized surface backscatter cross section (2A21), etc. Some of these variables do have a physical altitude, e.g. infrared temperatures are representative of the cloud top. Lateral displacements due to off-nadir TRMM scanning angles are ignored, even for the TMI which scans at a constant 53°. These quantities are interpolated to the EDOP profiles in an identical fashion to the PR data, as described in section A.3, using the Cressman weighting in (A6). The exception to this are discrete variables such as the rain type (2A23). For such quantities no interpolation can be performed and the TRMM pixel nearest the EDOP profile is used.

Appendix B: Simulating PR reflectivities using EDOP data

B.1 Technique

The simulation of spaceborne data using airborne radar data has been discussed by Amayenc et al. (1996) and Durden et al (1998), and a similar technique is used here. First, EDOP data are corrected for aircraft motion. In particular, changes in aircraft pitch renders the beams non-equidistant. Strictly speaking an inverse convolution of the EDOP data is needed to remove the effects of EDOP range resolution, however EDOP's resolution is high enough compared to that of the PR to treat EDOP data as representative of a point. The next step in the simulation involves a convolution of the EDOP data with a 1D (along-track) Gaussian weighting function. Finally, a reflectivity threshold is applied, reflecting the limited sensitivity of the PR. Differences in frequency between the PR and EDOP lead to differences in attenuation. It is assumed that the PR attenuation correction (Iguchi and Meneghini 1994) is accurate and that EDOP reflectivities are not significantly attenuated, in other words no further attenuation correction is performed in the simulation process. Also, the effect of decreasing vertical resolution of the PR with increasing scanning angle is ignored, and the degraded EDOP data have a 250 m vertical resolution independent of incidence angle.

B.2 Limitations of degraded EDOP data as a surrogate for PR data

There are limitations to the representativeness of degraded EDOP reflectivities as surrogate PR data. A perfectly 'degraded' EDOP section will normally not perfectly match the corresponding PR section for two reasons: lack of high-resolution information about the third dimension (i.e. across the flight track of the ER-2), and non-simultaneity of the observations. Simultaneous records will compare poorly when reflectivity contours (on a map) are tightly packed along an ER-2 flight leg, i.e. when the ER-2 flies along precipitation systems, rather than across them. The radar maps in Figure 3, as well as passive visible, infrared and microwave data from scanning instruments on the ER-2 can be used to assess cross-track variability. Non-simultaneity is often a more serious problem: for instance it takes the ER-2 about 8 minutes to sample a 100 km long storm, while it takes the TRMM satellite about 14 seconds to travel the same distance (Table 1). Poor comparisons can be expected from rapidly evolving storms, and when a high reflectivity gradient is advected across an ER-2 flight leg. Small thunderstorms are especially difficult to compare because of NUBF and because they are typically short-lived. For larger (stratiform) systems a larger time lag between EDOP and the PR is acceptable.

References

Amayenc, P.M., J.P. Diguet, M. Marzoug, and T.Tani, 1996: A class of single- and dual-frequency algorithms for rain-rate profiling from a spaceborne radar. Part II: Tests from airborne radar measurements. *J. Atmos. Oceanic Tech.*, **13**, 142-164.

Bolen, S.M. and V. Chandrasekar, 1999: Comparison of satellite-based and ground-based radar observations of precipitation. Preprints, 29nd Conference on Radar Meteorology, Montreal, Canada, Amer. Meteor. Soc., 751-753.

Caylor, I. J., G. M. Heymsfield, S. W. Bidwell, and S. S. Ameen, 1995: Estimating the rain rate profile in the presence of attenuation using EDOP airborne radar observations. Preprints, 27th Radar Meteor. Conf., Amer. Meteor. Soc., Vail, 783-785.

Cressman, G. P., 1959: An operational objective analysis system. *Mon. Wea. Rev.*, **87**, 367-374.

Datta, S., B. Roy, L. Jones, T. Kasparis, P.S. Ray, Z. Ding, and D. Charalampidis, 1999: Evaluation of TRMM precipitation radar rainfall estimates using NEXRAD and rain gauges in Central and South Florida. Preprints, 29nd Conference on Radar Meteorology, Montreal, Canada, Amer. Meteor. Soc., 754-757.

Dodge, P., R.W. Burbee, and F.D. Marks, Jr.,1999: The kinematic structure of a hurricane with sea level pressure less than 900 mb. *Mon. Wea. Rev.*, **127**, 987-1004.

Donaldson, R. J. Jr., 1964: A demonstration of antenna beam errors in radar reflectivity patterns. *J. Appl. Meteor.*, **3**, 611-623.

Durden, S.L., Z.S. Haddad, A. Kitiyakara, and F.K. Li, 1998: Effects of non-uniform beam filling on rainfall retrieval for the TRMM precipitation radar. *J. Atmos. Oceanic Tech.*, **15**, 635-646.

Goldhirsh, J. and B. Musiani, 1986: Rain cell size characteristics derived from radar observations at Wallops Island, Virginia. *IEEE. Trans. Geosci. Remote Sens.*, **GE-24**, 947-954.

Heymsfield, G. M., K. K. Ghosh, and L. C. Chen, 1983: An interactive system for compositing digital radar and satellite data. *J. Clim. Appl. Meteor.*, **22**, 705-713.

____________, S. Bidwell, I. J. Caylor, S. Ameen, S. Nicholson, W. Boncyk, L. Miller, D. Vandemark, P. E. Racette, and L. R. Dod, 1996a: The EDOP radar system on the high altitude NASA ER-2 aircraft. *J. Atmos. Oceanic Tech.*, **13**, 795-809.

____________, I. J. Caylor, J. M. Shepherd, W. S. Olson, S. W. Bidwell, W. C. Boncyk, and S. Ameen, 1996b: Structure of Florida thunderstorms using high-altitude aircraft radiometer and radar observations. *J. Appl. Meteor.*, **10**, 1736-1762.

Houze, R.A., Jr. 1993: *Cloud dynamics*. Academic Press, 573 pp.

Iguchi,T. and R. Meneghini, 1994: Intercomparison of single-frequency methods for retrieving a vertical rain profile from airborne or spaceborne radar data. *J. Atmos. Oceanic Tech.*, **11**, 1507-1516.

Kozu, T. and T. Iguchi, 1999: Non-uniform beam-filling correction for spaceborne radar rainfall measurement: implication from TOGA/COARE radar data analysis. *J. Atmos. Oceanic Tech.*, accepted.

Kummerow, C., W. Barnes, T. Kozu, J. Shiue, and J. Simpson, 1998: The Tropical Rainfall Measuring Mission (TRMM) sensor package. *J. Atmos. Oceanic Tech.*, **15**, 809-817.

McGaughey, G., E.J. Zipser, R.W. Spencer and R.E. Hood, 1996: High-resolution passive microwave observations of convective systems over the tropical Pacific Ocean. *J. Appl. Meteor.*, **35**, 1921-1947.

Nakamura, K., 1991: Biases of rain retrieval algorithms for spaceborne radar caused by nonuniformity of rain. *J. Atmos. Oceanic Tech.*, **8**, 363-373.

NASDA, 1999: TRMM PR Algorithm Instruction Manual V1.0, 52 pp [available from: Communications Research Laboratory, 4-2-1 Nukui-kitamachi, Koganei-chi, Tokyo 184, Japan].

Sauvageot, H., F. Mesnard and R.S. Tenorio, 1999: The relation between the area-average rain rate and the rain cell size distribution parameters. *J. Atmos. Sci.*, **56**, 57-70.

Spencer, R., and Coauthors, 1994: High-resolution imaging of rain systems with the Advanced Microwave Precipitation Radiometer. *J. Atmos. Oceanic Tech.*, **11**, 849-857.

Steiner, M. R.A. Houze Jr., S.E. Yuter, 1995: Climatological characterization of three-dimensional storm structure from operational radar and raingauge data. *J. Appl. Meteor.*, **34**, 1978-2007.

Testud, J. , P. Amayenc, X.K. Dou and T.F. Tani, 1996: Tests of rain profiling algorithms for a spaceborne radar using raincell models and real data precipitation fields. *J. Atmos. Oceanic Tech.* **13**, 426-453.

Trapp R.J., and C.A. Doswell III, 1999: On the objective analysis of weather radar data. Preprints, 29nd Conference on Radar Meteorology, Montreal, Canada, Amer. Meteor. Soc., 248-251.

Wielicki, B.A., and R.M. Welch, 1986: Cumulus cloud properties derived using Landsat satellite radar. *J. Climate Appl. Meteor.*, **25**, 261-276.

Yuter, S. E., and R. A. Houze, Jr., 1995: Three-dimensional kinematic and microphysical evolution of Florida cumulonimbus. Part II: Frequency distributions of vertical velocity, reflectivity, and differential reflectivity. *Mon. Wea. Rev.*, **123**, 1941-1958.

Zawadski, I., F. Fabry, R. de Elia, A. Caya and P. Vaillancourt, 1999: On quantitative interpretation of radar measurements. Preprints, 29nd Conference on Radar Meteorology, Montreal, Canada, Amer. Meteor. Soc., 784-786.

Table 1. A comparison of some EDOP and TRMM PR parameters.

	EDOP	TRMM PR
Frequency (GHz)	9.6	13.8
Wavelength (cm)	3.12	2.17
Antenna	fixed, nadir and forward (34°)	scanning to ±17°
Footprint at 5 km altitude (km)	0.76	4.3
Beam spacing (km)	0.1	~4.3
Range resolution (m)	37.5	250*
Time required to sample a 100 km wide storm (along-track)	~8 min	~14 s
Minimum detectable signal (dBZ) at 5 km altitude.	-5	18
Number of indep. samples per pixel	~300	64

* 125 m at incidence angles less than 3.55°.

Table 2. Definition of TRMM PR rain types as a combination of the outcome of two tests, the H method and the V method. The order of the listing is the same as that in the lower right corner of Figures 4-9.

PR rain type	stratiform	convective	inconclusive
Strat cert	H,V		
Strat cert	V		H
Prob Strat	H		V
Maybe Strat	V	H	
Convect cert		H,V	
Convect cert		H	V
Convect cert		V	H
Prob Convect		H	V
Maybe Convect	H	V	
Maybe Convect	V (BB not clear)	H	
Others			H,V

Table 3. List of events with quasi-coincident TRMM-EDOP observations. Times are in UTC. The EDOP times are the start/end of a straight-and-level flight leg. The TRMM overpass time over the domains shown in Figure 3 may take 10-30 seconds, but the time closest to the PR coverage of the feature of interest is shown. The ground-based radar time is the start time of a volume scan.

Date	Type of Event	EDOP	TRMM	Ground Radar
21 April '98	frontal - mostly stratiform	06:24 - 06:45	06:33:45	KFWS 06:36:46
13 August '98	decaying convective cell	22:25 - 22:30	22:29:52	S-POL 22:25:06
1 February '99	growing convective cell	18:17 - 18:21	18:25:47	S-POL 18:16:00
23 February '99	small MCS	20:56 - 21:03	21:00:47	TOGA 21:00:19
26 August '99	Hurricane Bonnie (Pass 1)	11:41 - 12:13	11:37:16	KLTX 11:36:10
26 August '99	Hurricane Bonnie (Pass 3)	14:47 - 15:12	14:50:30	KLTX 14:55:03

Figure Captions

Figure 1. A comparison of the PR, EDOP and ground radar geometries.

Figure 2. Scale dependency of PR reflectivity estimates. The curves in (a) show the variation of PR-measured reflectivity as a function of the storm cell size, for various cell locations relative to the center of the PR footprint. The horizontal shape of the storm cell is assumed to be bell-shaped with a maximum reflectivity of 50 dBZ. The PR beam illumination function is also assumed to be Gaussian. The PR-estimated rainrate is shown in (b) for the same conditions.

Figure 3. Reflectivities from TRMM PR and ground-based radar mapped to common earth coordinates. The left panel for each case (3a, c, e, g, i, and k) provides the 2 km altitude 2A25 product. The right panel (3b, d, f, h, j, and l) displays the lowest clutter-free radar elevation scan from the various radars. The ER-2 flight track with start and end times (UTC) is indicated on the plot. Values exceeding 50 dBZ are shown white, values less than 0 dBZ are black, and the background is gray. The 'X' denotes the location of the relevant ground radar.

Figure 4. Composite of vertical reflectivity sections from (a) EDOP, (b) ground radar, and (c) the PR, for 21 April 1998, mapped to coordinates of EDOP cross section (top panel). Panel (d) shows a 'degraded' EDOP section, simulating the PR (Appendix B). The time difference (Dt) between the EDOP profile and the PR overpass is labeled below the EDOP image in minutes, where positive numbers indicate that the EDOP vertical profile is later than the TRMM image. Panels (e-g) show various TRMM products corresponding to this cross section. TMI microwave brightness temperatures at 10, 19, 35, and 85.5 GHz, together with the VIRS infrared brightness temperature,

are shown in panel (e). PR-derived storm top and BB heights are shown in panel (f), and the rain type classification is shown in panel (g) together with the PR incidence angle.

Figure 5. As Fig. 4, but for 13 August 1998.

Figure 6. As Fig. 4, but for 1 February 1999.

Figure 7. As Fig. 4, but for 23 February 1999. The TRMM simulation by means of EDOP data is omitted, instead a reflectivity cross-section from a second ground radar is shown.

Figure 8. As Fig. 4, but for 26 August 1998 (pass 1).

Figure 9. As Fig. 4, but for 26 August 1998 (pass 3).

Figure 10. Mean reflectivity profiles derived from the vertical cross sections in Figures 4-9. The averages are calculated over the entire section, except were shown (i.e. for 13 August). Ground radar profiles are identified also by the start time of the volume scans. (a) 21 April 1998; (b) and (c), 13 August 1998; (d) 1 February 1999; (e) 23 February 1999; and (f) 26 August 1998.

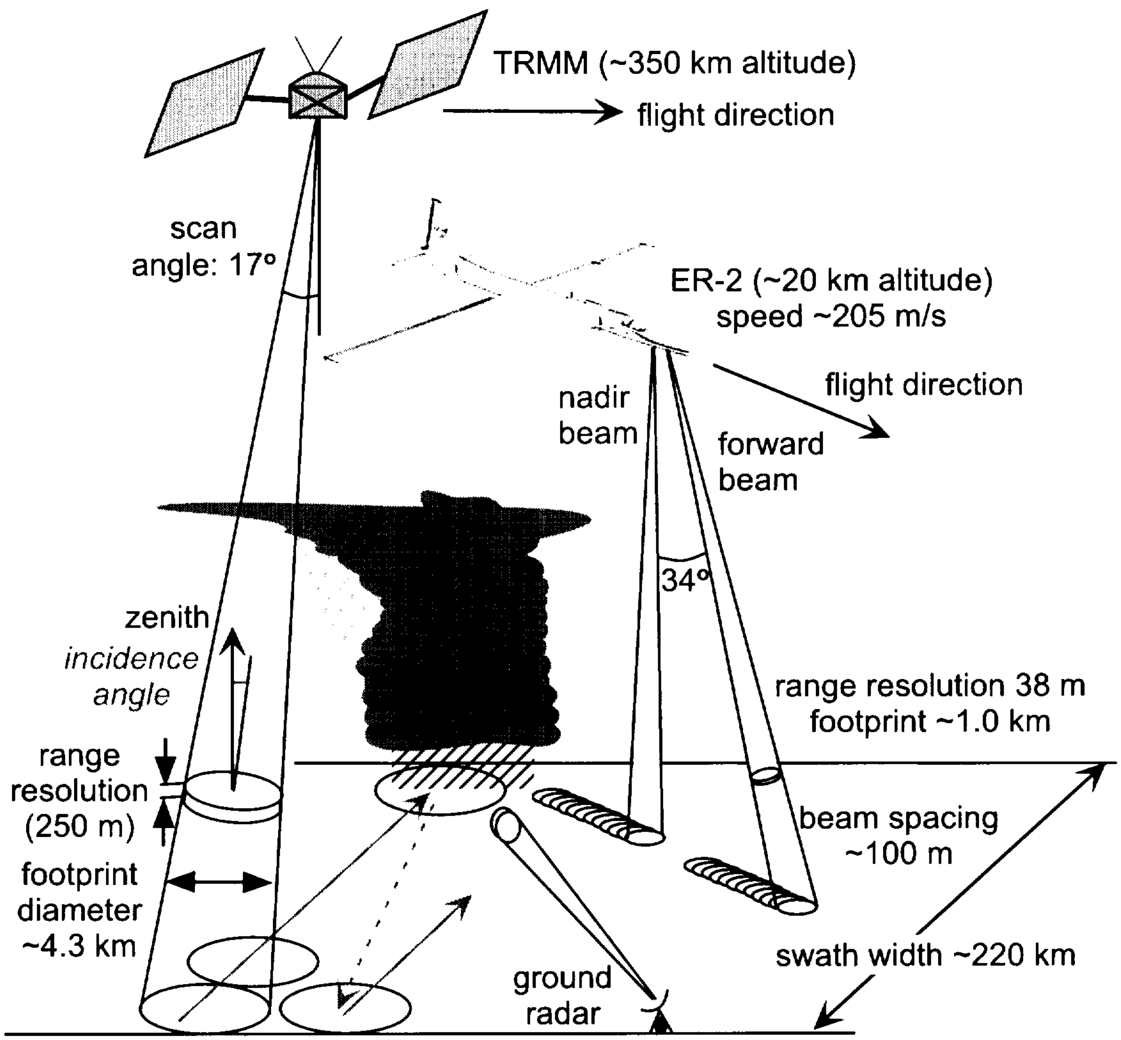
TRMM (~350 km altitude)
flight direction
scan
angle: 17°
ER-2 (~20 km altitude)
speed ~205 m/s
flight direction
nadir
beam
forward
beam
34°
zenith
incidence
angle
range
resolution
(250 m)
footprint
diameter
~4.3 km
range resolution 38 m
footprint ~1.0 km
beam spacing
~100 m
swath width ~220 km
ground
radar

1

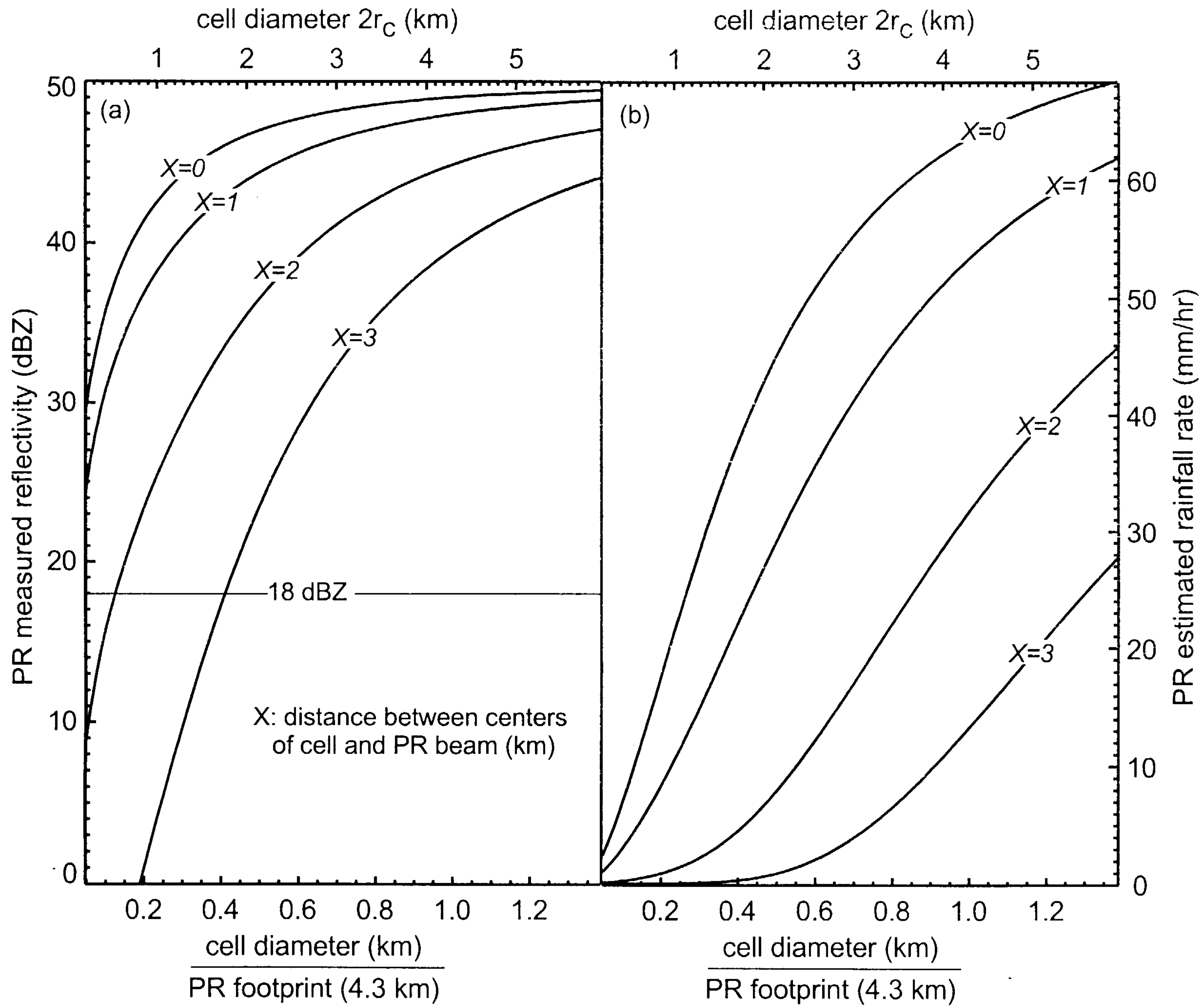
cell diameter 2rC (km)
(a)
(b)
X=0
X=1
X=2
X=3
18 dBZ
X: distance between centers of cell and PR beam (km)
PR measured reflectivity (dBZ)
PR estimated rainfall rate (mm/hr)
cell diameter (km) / PR footprint (4.3 km)

2

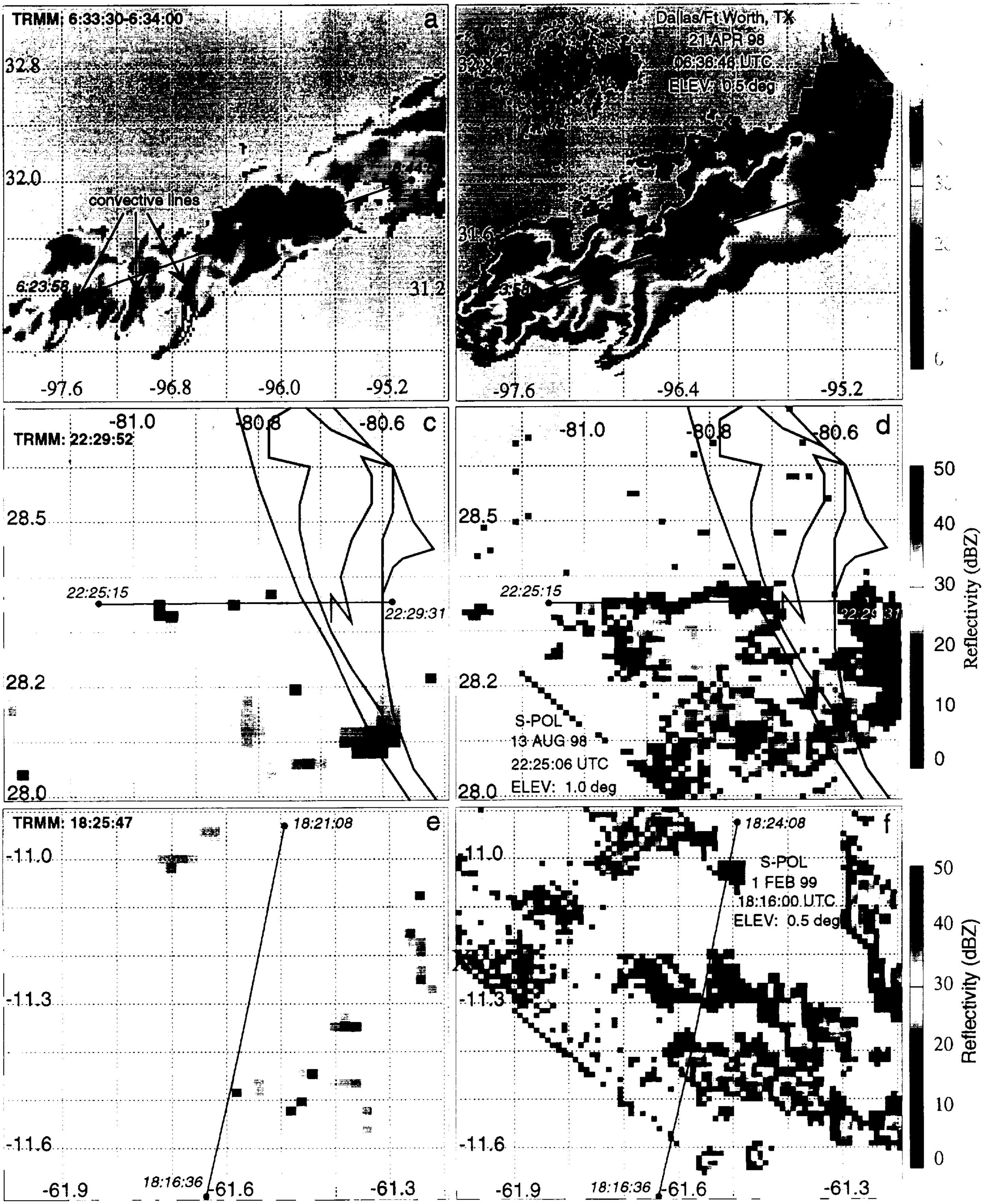
TRMM: 6:33:30-6:34:00
a
32.8
32.0
convective lines
6:23:58
31.2
-97.6
-96.8
-96.0
-95.2
Dallas/Ft Worth, TX
21 APR 98
06:36:46 UTC
ELEV: 0.5 deg
-97.6
-96.4
-95.2
TRMM: 22:29:52
c
-81.0
-80.8
-80.6
28.5
22:25:15
22:29:31
28.2
28.0
d
S-POL
13 AUG 98
22:25:06 UTC
ELEV: 1.0 deg
50
40
30
20
10
0
Reflectivity (dBZ)
TRMM: 18:25:47
e
18:21:08
-11.0
-11.3
-11.6
18:16:36
-61.9
-61.6
-61.3
f
18:24:08
S-POL
1 FEB 99
18:16:00 UTC
ELEV: 0.5 deg

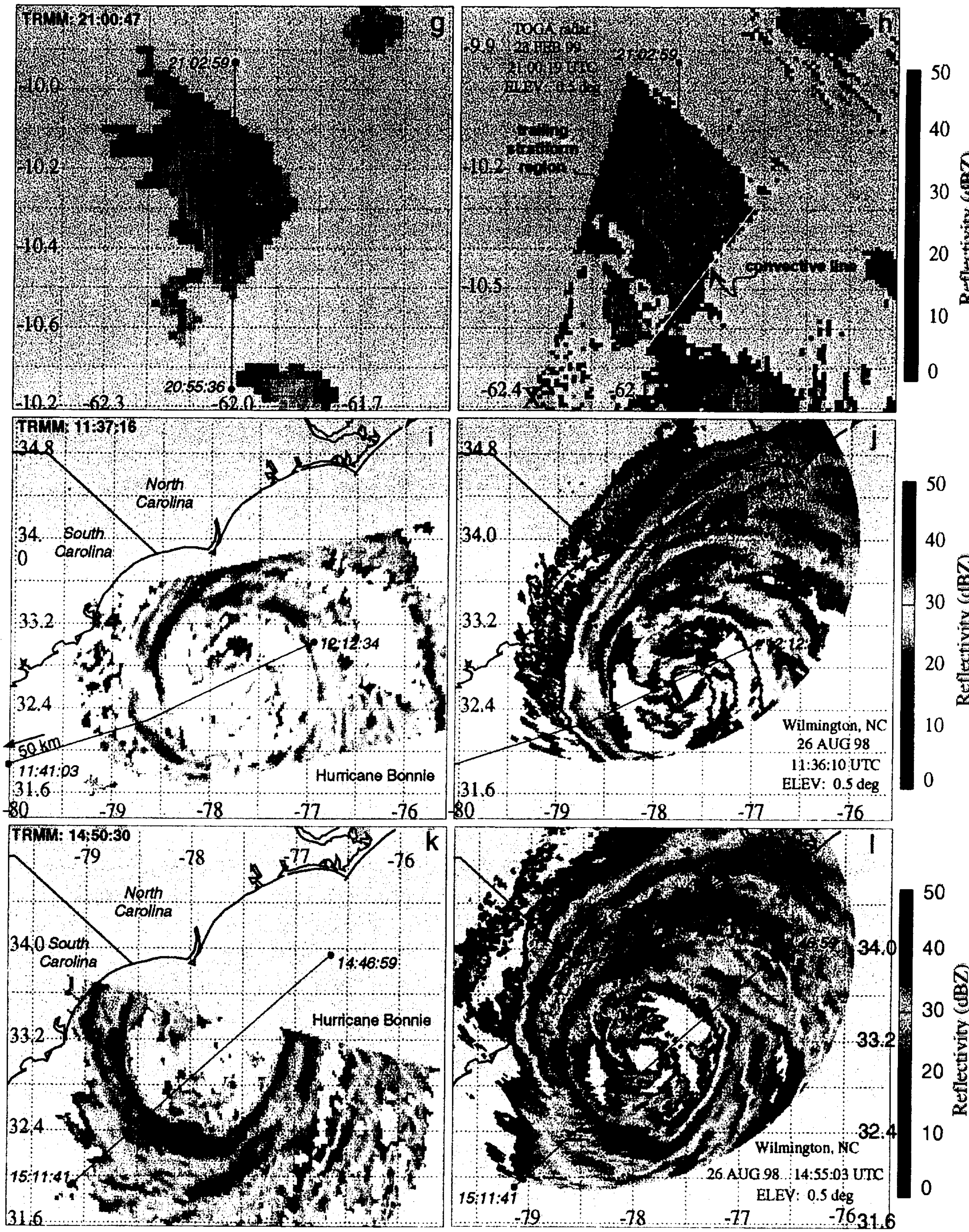

TRMM: 21:00:47
g
21:02:59
20:55:36
h
TOGA radar
28 FEB 99
ELEV: 0.5 deg
21:02:59
trailing
stratiform
region
convective line
Reflectivity (dBZ)
TRMM: 11:37:16
i
North
Carolina
South
Carolina
12:12:34
50 km
11:41:03
Hurricane Bonnie
j
Wilmington, NC
26 AUG 98
11:36:10 UTC
ELEV: 0.5 deg
TRMM: 14:50:30
k
North
Carolina
South
Carolina
14:46:59
Hurricane Bonnie
15:11:41
l
Wilmington, NC
26 AUG 98 14:55:03 UTC
ELEV: 0.5 deg
15:11:41

3

TEFLUN-A 21 April 1998

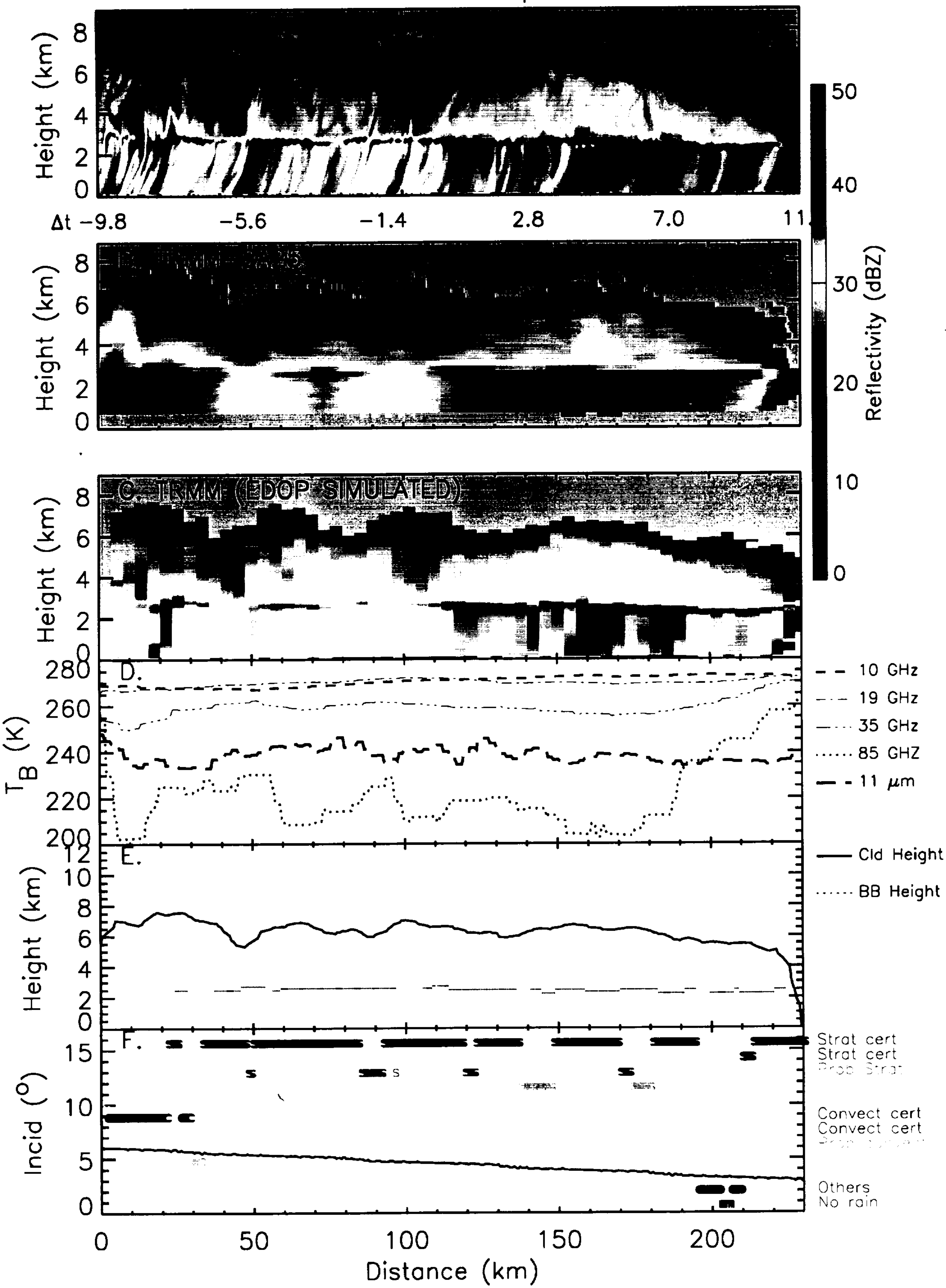

4

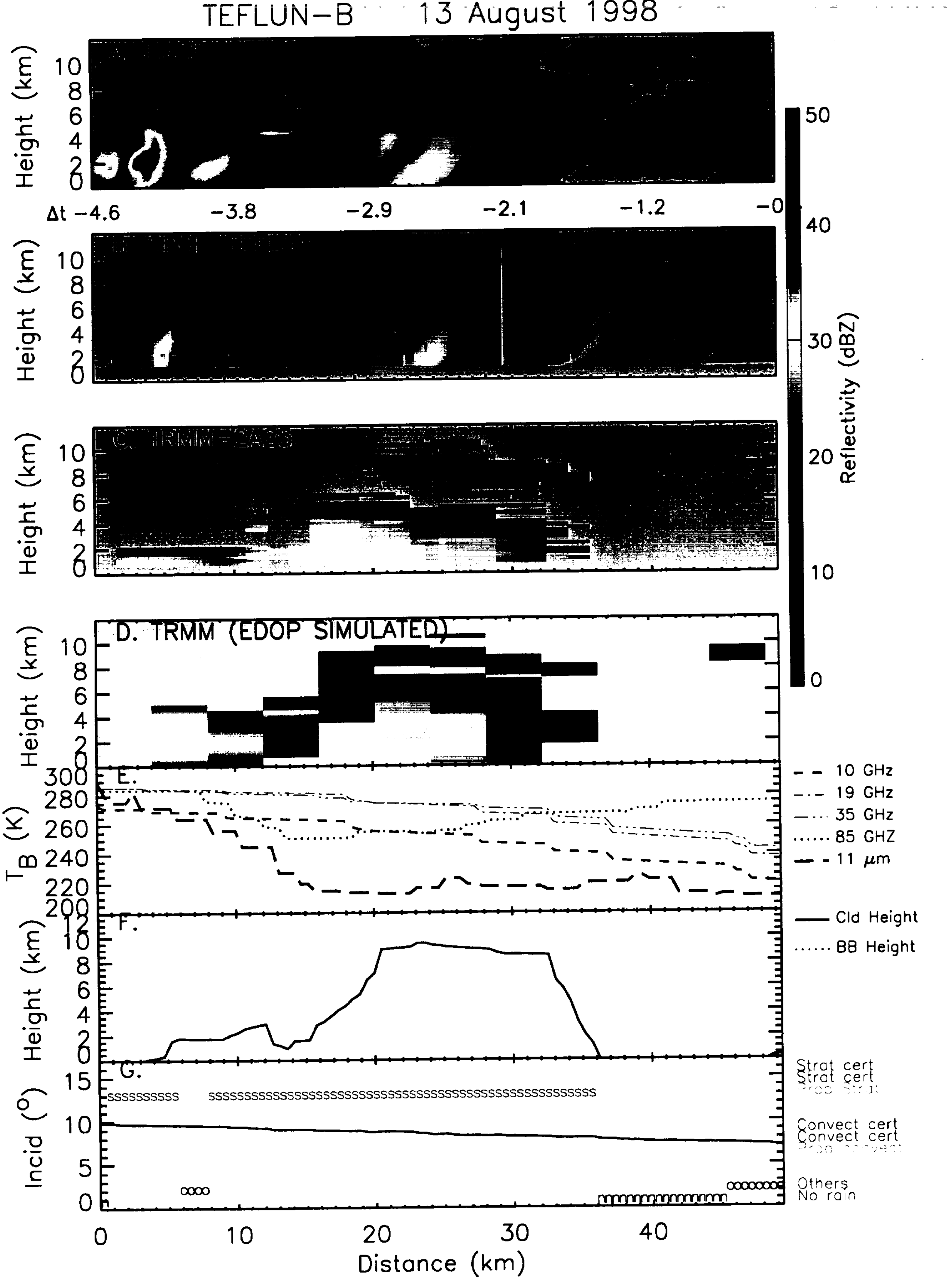

TEFLUN-B 13 August 1998
Height (km)
Δt -4.6
-3.8
-2.9
-2.1
-1.2
-0
C. TRMM-2A25
D. TRMM (EDOP SIMULATED)
Reflectivity (dBZ)
E.
T_B (K)
10 GHz
19 GHz
35 GHz
85 GHZ
11 μm
F.
Cld Height
BB Height
G.
Incid (°)
Strat cert
Convect cert
Others
No rain
Distance (km)

5

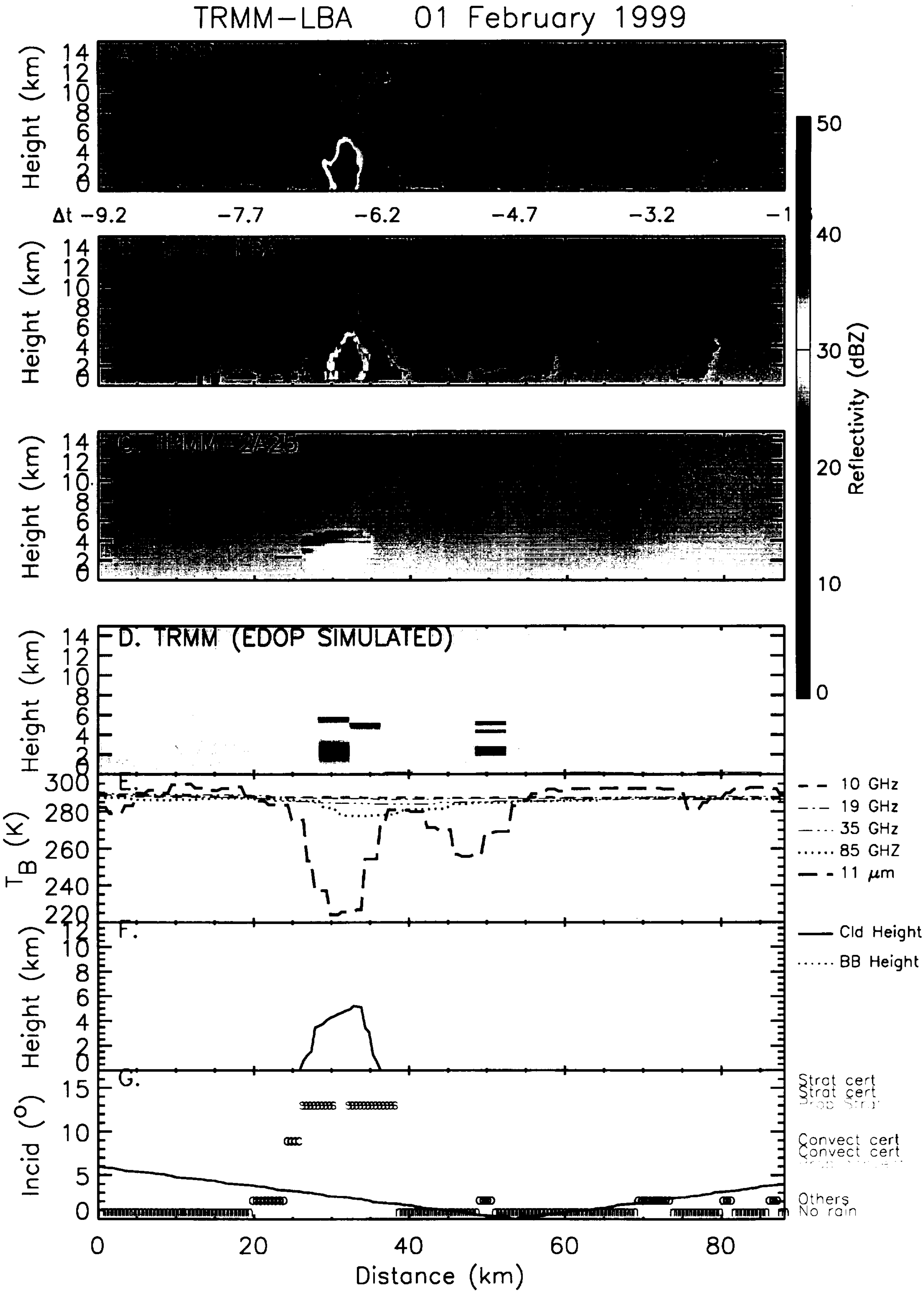
TRMM-LBA 01 February 1999
Height (km)
Δt −9.2
−7.7
−6.2
−4.7
−3.2
C. TRMM 2A25
D. TRMM (EDOP SIMULATED)
Reflectivity (dBZ)
50
40
30
20
10
0
E.
T_B (K)
10 GHz
19 GHz
35 GHz
85 GHZ
11 μm
F.
Cld Height
BB Height
G.
Incid (°)
Strat cert
Strat cert
Convect cert
Convect cert
Others
No rain
Distance (km)

TRMM-LBA 23 February 1999

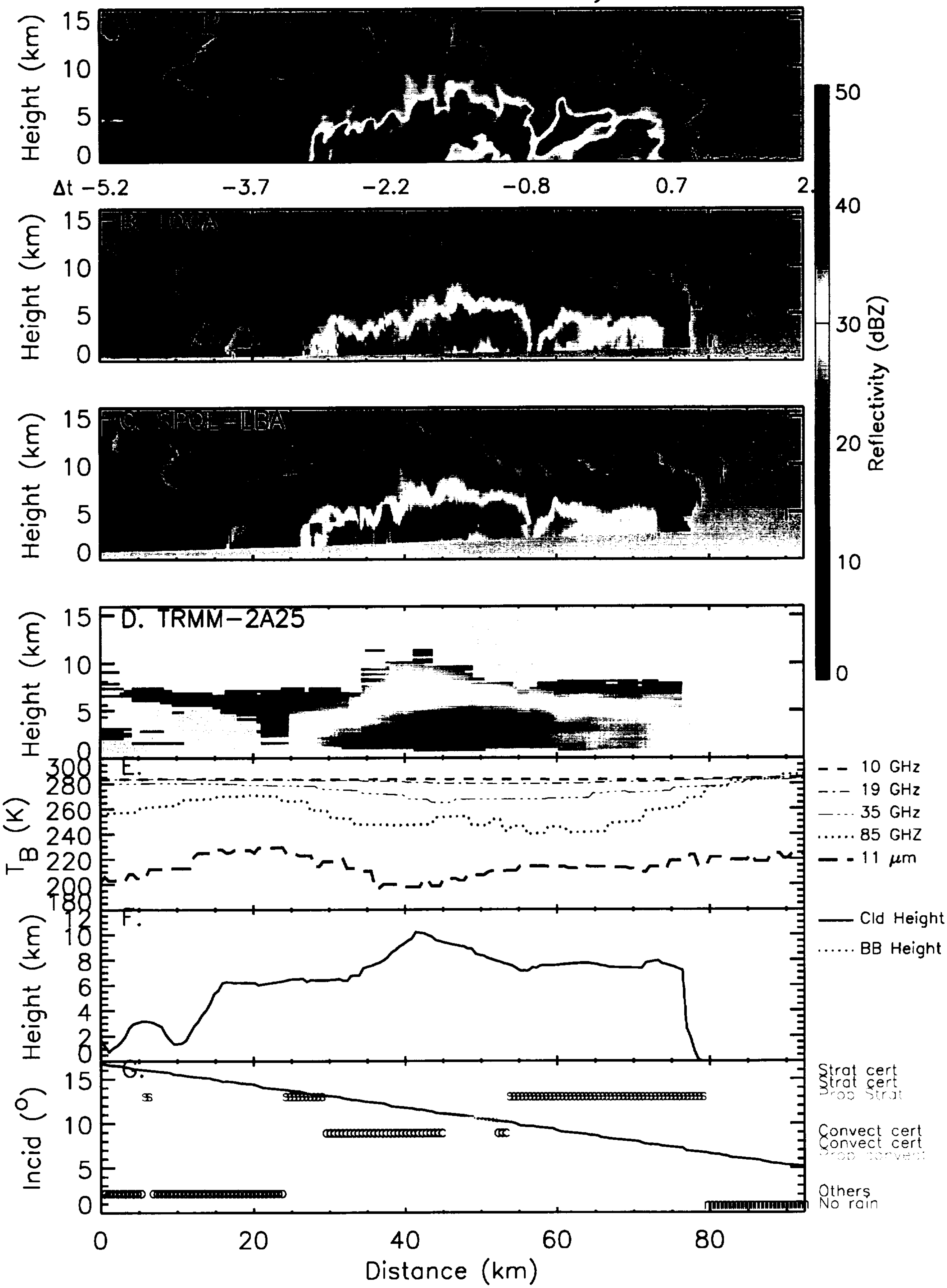

7

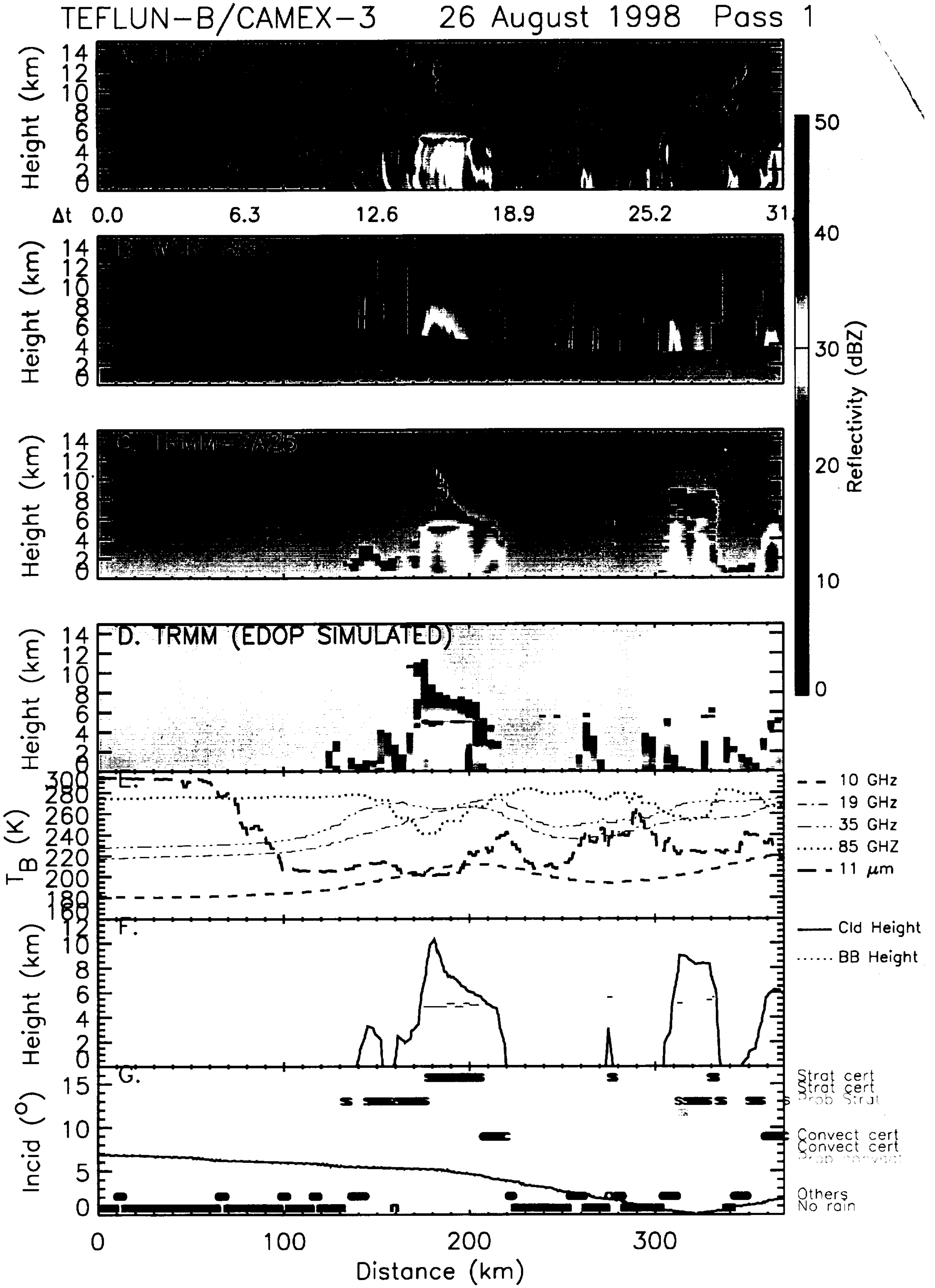
TEFLUN-B/CAMEX-3 26 August 1998 Pass 1
Height (km)
Δt 0.0 6.3 12.6 18.9 25.2 31
Reflectivity (dBZ)
D. TRMM (EDOP SIMULATED)
E.
T_B (K)
10 GHz
19 GHz
35 GHz
85 GHZ
11 μm
F.
Cld Height
BB Height
G.
Incid (°)
Strat cert
Strat cert
Prob Strat
Convect cert
Convect cert
Others
No rain
Distance (km)

TEFLUN-B/CAMEX-3 26 August 1998 Pass 3

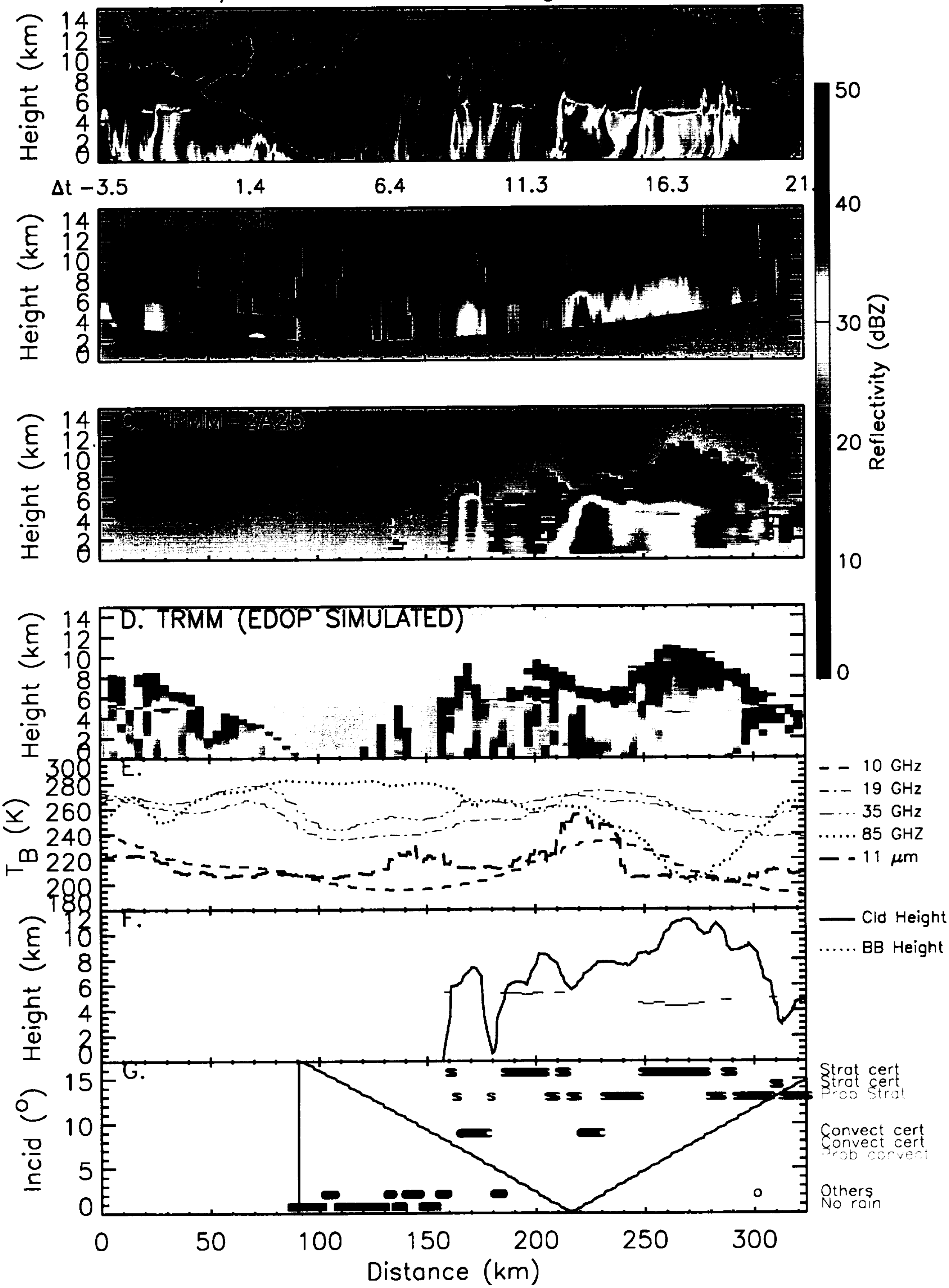

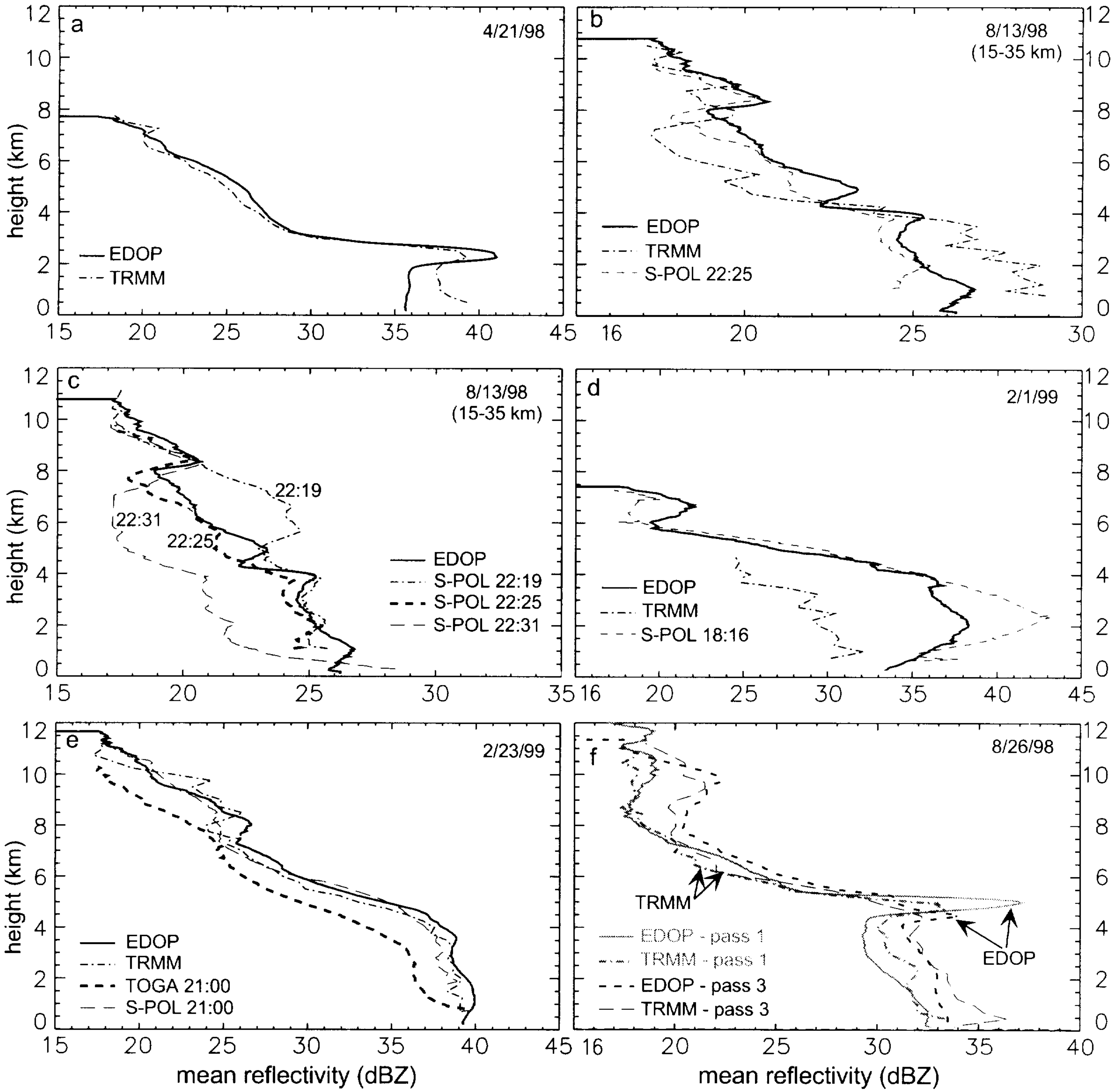

a
4/21/98
EDOP
TRMM
b
8/13/98
(15-35 km)
EDOP
TRMM
S-POL 22:25
c
8/13/98
(15-35 km)
22:19
22:31
22:25
EDOP
S-POL 22:19
S-POL 22:25
S-POL 22:31
d
2/1/99
EDOP
TRMM
S-POL 18:16
e
2/23/99
EDOP
TRMM
TOGA 21:00
S-POL 21:00
f
8/26/98
TRMM
EDOP
EDOP - pass 1
TRMM - pass 1
EDOP - pass 3
TRMM - pass 3
height (km)
mean reflectivity (dBZ)